EFFECTS OF MILLISECOND SCALE LASER SPIKE ANNEALS ON AMORPHOUS BARIUM TITANATE THIN FILMS

A Thesis

Presented to the Faculty of the Graduate School

of Cornell University

In Partial Fulfillment of the Requirements for the Degree of

Master of Science

by

Lewis Rosevere Haber

May 2019

ABSTRACT

Barium titanate is the most widely used dielectric material for ceramic capacitors. The perovskite phase, in particular is prized for its high, stable dielectric constant across a wide temperature range. In addition to the five observed crystalline phases, computational materials science suggest that there exist many more unobserved metastable phases. In this study, amorphous barium titanate films deposited at room temperature on Si substrates via pulsed laser deposition or sputtering were annealed with a CO_2 laser in air, achieving peak temperatures from 600-1300 ℃ and dwell times from 250-10000 μs. The samples were then analyzed with synchrotron x-ray diffraction, optical reflectometry and optical microscopy. The laser spike anneal induced surface roughening and delamination in films annealed above 780 ℃. This roughening is consistent with the formation of a low density amorphous phase before crystal nucleation, causing film delamination. Diffraction analysis revealed the onset of crystallization strongly coincided with film damage. Crystallization produced both the equilibrium tetragonal phase and the metastable hexagonal phases. Short anneals near the crystallization threshold produced pure tetragonal regions, while all other anneals above the threshold produced mixed hexagonal and tetragonal regions. These data show that millisecond scale laser spike anneals show promise as a method to stabilize metastable phases in thin films.

BIOGRAPHICAL SKETCH

The author, Lewis Haber, was born and raised in Urbana, Illinois, just off the campus of the University of Illinois at Urbana-Champaign. He attended public schools locally until graduating from Urbana High School in 2014. He then moved to Ithaca, New York to pursue higher education at the Cornell University College of Engineering, majoring in Materials Science & Engineering beginning in Fall of 2014. During his time at Cornell University, Lewis actively participated in the Cornell Big Red Marching Band, and served as Tuba Section leader for the 2016 season. Beginning in the Spring of 2017, he joined a team of research consultants providing services for Applied Materials, Inc. under the guidance of Prof. Robert B. van Dover. He began studying the effects of laser spike anneals on barium titanate as for his senior thesis project. After graduating with his Bachelor of Science in Spring of 2018, Lewis continued his research on barium titanate in order to pursue a Master of Science from Cornell University, which was conferred upon him in Spring of 2019. After his time at Cornell University, Lewis moved to Knoxville, Tennessee to develop thin film semiconductor technology for Lux Semiconductors in partnership with Oak Ridge National Laboratories

ACKNOWLEDGEMENTS

Firstly, I would like to thank my advisor, Prof. Robert B. van Dover. My first steps into materials research were in your lab, and your expertise and guidance have made me never question my choice in research area. Additionally, my work on the Applied Materials project would not have been possible without your charitable time contributions every week. Although leaving after these three years is bittersweet, I look forward to reading about the great achievements that will occur in years to come.

Prof. Michael Thompson, thank you for all the hard work you do for the MSE department and your research group. This thesis would not have been possible without your ingenious GENPLOT and LASGO contraptions. Additionally, my undergraduate education would have been incomplete without your gauntlet of courses.

Thank you Aine Connolly and Emily Cheng for your assistance during laser spike anneals. Peter Beaucage, thank you for your expert guidance during synchrotron data collection and analysis. Sebastian Ament, I would like to thank you and the Gomes group for the sneak peek at your outstanding background subtraction algorithm. Duncan Sutherland, Max Amsler, Katherine Quinn, Vidit Gupta and Juliane Scholtz: thank you for livening up the Duffield Office and making work a fun place to be. Gary Chen, I'll look back on our AMAT work almost as fondly as our afternoon philosophical discussions.

This thesis would not have been possible without the outstanding facilities and advice provided by the Cornell Nanoscale Facility and the Cornell Center for Materials Research.

Table of Contents

LIST OF FIGURES

LIST OF TABLES

LIST OF ABBREVIATIONS AND SYMBOLS

CO_2: Carbon Dioxide

$BaTiO_3$: Barium titanate.

p-BTO: Perovskite-structure barium titanate.

Ti: Titanium

°C: Degrees Celsius

nm: nanometer, 10^{-9} meters

h-BTO: hexagonal barium titanate

Ba: Barium

a-BTO: amorphous barium titanate

FeRAM: Ferroelectric Random Access Memory

s: second.

CVD: Chemical Vapor Deposition.

PVD: Physical Vapor Deposition.

PLD: Pulsed Laser Deposition.

CCMR: Cornell Center for Materials Research

Ar: Argon

mTorr: millitorr, 10^{-3} Torr

O: Oxygen

W: Watt

lgLSA: lateral gradient Laser Spike Anneal.

µm: micrometer, 10^{-6} meters

Ω: Ohm

cm: centimeter 10^{-2} meters

Si: Silicon

K: Kelvin

ms: Millisecond 10^{-3} seconds.

λ: Electromagnetic radiation wavelength.

d: Interatomic plane spacing.

θ: Diffraction angle.

XRD: X-ray Diffraction.

Å: Angstrom, 10^{-10} meters.

τ: Average crystal domain size.

β: Peak full width half maximum.

CHESS: Cornell High Energy Synchrotron Source.

MeV: Mega electron Volts, 10^{6} electron volts.

GeV: Giga electron Volts 10^{9} electron volts.

OPD: Optical Path Distance.

d_{film}: film thickness.

n_{film}: film refractive index.

μs: microsecond, 10^{-6} seconds.

“: inch

Hz: Hertz

Ra: Arithmetic average roughness.

RF: Radio frequency.

DC: Direct Current

IPA: Isopropyl alcohol.

°: degrees

2θ: Two theta diffraction angle, twice the diffraction angle.

AC: Alternating Current

g: grams

mol: mole, $6.023x10^{23}$

EDS: Energy Dispersive x-ray Spectroscopy.

XPS: X-ray Photoelectron Spectroscopy.

LSA: Laser Spike Anneal.

SiO_2: Silicon Dioxide

q: scattering vector

q-length: magnitude of scattering vector

Zr: Zirconium

CHAPTER 1: INTRODUCTION

Introduction to the Barium Titanate Materials System

Since its discovery during the Second World War, barium titanate ($BaTiO_3$) has found applications in a wide variety of applications. As the first known ferroelectric oxide, $BaTiO_3$ paved the way for a class of materials critical to the function of several electronic technologies. In addition to ferroelectricity, $BaTiO_3$ is pyro and piezoelectric. It is currently the most common dielectric material used in multilayer ceramic capacitors, being involved in the manufacture of over 10^{12} devices per year [1]. In this application, $BaTiO_3$ is prized for its high dielectric constant of over 1000, and its low dielectric loss of less than 1% [2]. In most applications, $BaTiO_3$ exists in its thermodynamic equilibrium perovskite polymorph (p-BTO). Figure 1.1 provides a visualization of the unit cell for this polymorph. At standard temperatures and pressures, p-BTO forms a tetragonal crystal system. In this case, the central Ti^{4+} cation is displaced slightly along one axis in its oxygen octahedra. This displacement gives rise to a polarization in the unit cell, which results in the ferro-, piezo- and pyroelectric properties in $BaTiO_3$. Above 120 °C, p-BTO exists as a cubic crystal system. While the Ti^{4+} cation actually undergoes a <1 1 1> distortion in its octahedra, thermal energy allows for continuous switching between all eight possible distortion directions [3]. As a result, the time-averaged crystal system is centrosymmetric cubic

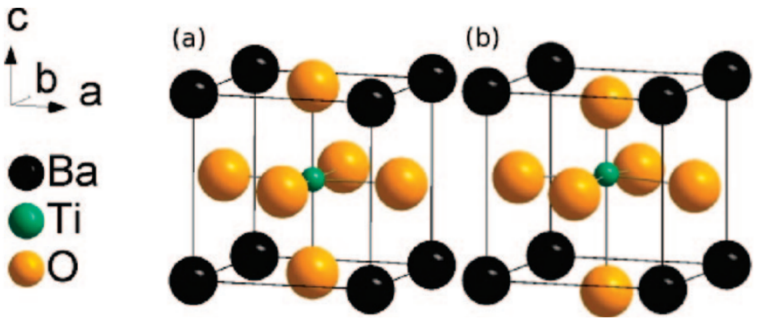

Figure 1.1: Unit cells of p-BTO. (a) shows the cubic phase while (b) shows the tetragonal phase. Adapted from [1].

with no net polarization and hence is neither ferro-, piezo- or pyroelectric. Below 5 °C, the unit cell undergoes a <1 1 0> distortion and becomes orthorhombic. Below 90 °C the unit cell undergoes a <1 1 1> distortion and becomes rhombohedral. Anomalies in the dielectric constant occur around these transition temperatures. In applications where $BaTiO_3$ is used as a dielectric, these phase transitions are undesirable as they cause rapid changes in capacitance. Therefore, $BaTiO_3$ is commonly doped to increase the phase stability in common operating temperature regimes [4]. A major drawback of this approach is an inherently limited temperature operating regimes; phase transition temperatures can only be elevated or depressed, never removed. Moreover, the inclusion of dopants can reduce the dielectric constant of $BaTiO_3$. Grain size has also shown to have a marked effect on the crystal structure of p-BTO. As grain size decreases, differential scanning calorimetry shows that the stability window for tetragonal $BaTiO_3$ decreases in turn. Around grain sizes of 35 nm, the orthorhombic to tetragonal and tetragonal to cubic transitions vanish. However, Raman spectroscopy shows that the material possesses orthorhombic and cubic phonon modes at room temperature [5]. Further studies suggest that reduced grain sizes result in a coexistence of cubic, tetragonal and orthorhombic phases across a broad temperature range [1]. Since grain boundaries act as “dead layers” in dielectric materials, nanograin $BaTiO_3$ is a rather poor dielectric material. However, the lack of discrete phase transitions would improve dielectric stability across a wide temperature range. Grain size control may prove to be an effective alternative to doping for dielectric stabilization.

$BaTiO_3$ also exists at high temperatures in a hexagonal polymorph, h-BTO, shown in Figure 1.2. This phase diverges from the perovskite structure as several Ti octahedra become face sharing. Since h-BTO is centrosymmetric, it does not possess the ferro-, piezo- and pyroelectric properties of p-BTO. There exist a number of methods to stabilize h-BTO at standard temperature and pressure. Doping the material with +3

acceptor species is the most commonly taken approach in literature [6] [7]. Additionally, if p-BTO crystals are fired in a reducing atmosphere, oxygen deficient h-BTO can be stabilized at room temperature [8] [9]. If fired again in a oxidizing atmosphere, stoichiometric h-BTO will remain stable at room temperature [10]. It has also been observed that h-BTO forms when amorphous, self-supported $BaTiO_3$ samples are annealed [11]. While it is considerably less researched than its perovskite cousin, h-BTO demonstrates several interesting properties that motivate further research. The only phase transitions in h-BTO occur at cryogenic temperatures. Therefore, it does not suffer from the same dielectric anomalies as p-BTO and is better suited for high and low temperature applications. Additionally, the dielectric constant for h-BTO has been measured to be on the order of 10^5 [6][12]. As current methods used to produce h-BTO tend to introduce electronic defects, most h-BTO is semiconducting. This limits its immediate applicability as a dielectric material due to possible current leakage. However, non-semiconducting h-BTO may prove to be an invaluable dielectric material.

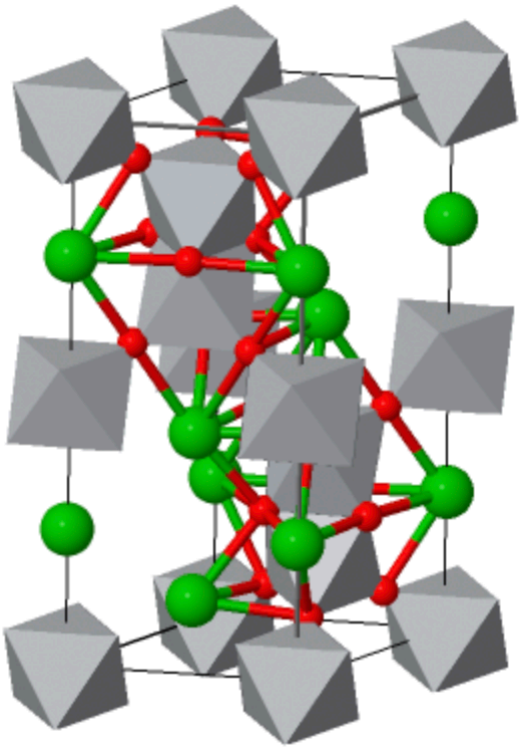

Figure 1.2: Structure of h-BTO. Oxygen atoms are shown in red, Ba in green, and Ti as grey octahedra.

A third solid form of $BaTiO_3$ is the amorphous phase, a-BTO. Unlike h-BTO and p-BTO, this phase lacks crystalline order. Instead, it can be described as a random network of face, edge and corner sharing Ti^{4+} octahedra, with Ba^{2+} ions

interspersed to balance charges [13]. Unlike its crystalline cousins, a-BTO has a rather poor dielectric constant that ranges from 10-20 [14]. As such, it is not a serious candidate for dielectric layers in capacitors. However, an interesting phenomenon associated with a-BTO is its ability to acquire a macroscopic polarization without adopting a crystal structure. Before crystallization, a-BTO undergoes a sharp volume expansion [15]. This expansion is believed to be the breaking of face and edge sharing bonds between Ti octahedra [16]. When this expansion is frustrated by substrate clamping, these bonds can preferentially break upon a strain gradient [17] [18]. This process can align the dipole moments in Ti octahedra, resulting in macroscopic polarization. This results in pyro- and piezoelectric amorphous thin films. Additional studies have showed that these films also possess ferroelectric properties [19]. These films are shown to retain their polarization and electrical properties up to crystallization temperatures around 800 °C. Thus, polar a-BTO may be a practical materials system in a high temperature sensor, FeRAM dielectric or piezoelectric actuator.

In addition to these three polymorphs, computational materials science predicts 11 stable crystalline phases of $BaTiO_3$ [19] [20]. Four of these phases have not been experimentally observed. These novel phases are not only potential new useful materials, but also could lead to discovery of similar phases in other perovskite systems similar to $BaTiO_3$.

To conclude, $BaTiO_3$ is known to exist as a solid in three forms: equilibrium p-BTO, high temperature h-BTO and metastable a-BTO. $BaTiO_3$ has already found widespread use as a dielectric material in capacitors due to its high dielectric constant and low dielectric lost. However, h-BTO may prove to be an even better dielectric material because of its superior dielectric constant and lack of phase transitions. Only recently discovered, a-BTO can acquire a macroscopic polarization stable to high

temperatures. It may prove useful in high temperature applications such as temperature sensing, FeRAM and piezoelectric actuators. Lastly, computational materials science suggests that at least four novel phases of $BaTiO_3$ may exist. For these reasons, $BaTiO_3$ was selected as the materials system of interest for this study.

Aim of Study

This study aims to explore the effects of millisecond scale laser spike anneals on amorphous $BaTiO_3$ thin films. From literature, $BaTiO_3$ has exhibited seven stable crystalline phases. Computational materials science suggests that four additional unobserved crystalline phases may also be stable. This high number of observed and predicted crystalline phases, in addition to the relatively complicated amorphous-crystalline transition, suggest that the energy landscape for $BaTiO_3$ is rugged. In other words, there exist several stoichiometric atomic arrangements that occupy energy minima and may form long lasting metastable phases. This study will aim to stabilize metastable phases through quenching. Two mechanisms may produce such a result in this experiment. Firstly, should an intermediate crystalline phase form as the amorphous phase transitions to the p-BTO or h-BTO polymorphs, a rapid quench may be able to lock in this transition phase at a low temperature. An additional possibility is the quenching in of the high temperature h-BTO phase. This may result in the stabilization of stoichiometric h-BTO at room temperature, or yield a different phase through a martensitic diffusionless transformation. Millisecond scale laser spike anneals will achieve heating and quench rates on the order of 10^4-10^6 °C/s, far exceeding typical rates for conventional furnace anneals.

Introduction to Mechanisms used for Study

1. Introduction to Physical Vapor Deposition Processes

In the microelectronics industry, a variety of methods exist to deposit thin films onto various substrates. Broadly speaking, the methods can be divided into Chemical Vapor Deposition (CVD) and Physical Vapor Deposition (PVD). CVD processes rely on combining at least two gaseous chemical compounds in a reaction chamber. Film growth is achieved by reacting these compounds on the substrate. PVD, on the other hand, relies on physical reactions to convert a material to vapor in a low pressure deposition chamber. This vapor can then travel through the chamber before condensing onto a substrate surface, resulting in film growth. The principal advantages of PVD over CVD are (i) simplicity, as one can use PVD to deposit most materials that exists as a bulk solid, (ii) and film purity, as side reactions and incomplete reactions can leave unwanted material in CVD-deposited films.

In order to create a vapor from a solid material, several techniques exist within the area of PVD. In this study, Pulsed Laser Deposition (PLD) and sputtering were employed. PLD relies on using a pulsed laser to ablate a given material from a solid source, known as a target, so that it deposits as a thin film on a substrate. To achieve laser fluences necessary to ablate materials, the spot size of the laser is typically much smaller than the target size. In comparison to sputtering, PLD systems are generally able to deposit films of greater stoichiometric fidelity to the target used. In this study, the Neocera Ex200 Pulsed Laser Deposition System in the Cornell Center for Materials Research (CCMR) was used to deposit thin films of barium titanate. The setup is shown in Figure 1.3 below, where the deposition side of the substrate is inverted and the laser ejects

material upwards from the target for deposition. Rotation of the substrate ensures radially symmetric film deposition. Additionally, the target itself is rotated and rastered back and forth. This target motion allows the laser to ablate from the entire surface of the target and ensures a uniform target surface free of burrows. In addition to depositions under high vacuum, depositions were also carried out in the presence of oxygen and argon. The presence of oxygen in the deposition atmosphere allows the deposited material to fully oxidize, decreasing the oxygen vacancy concentration. Argon was used as an inert gas to increase the overall working pressure. A higher deposition pressure results in more collisions between the chamber gas and the ejected materials, which thermalizes the plume of ejected materials, and increases film uniformity across the substrate [22]. The increased working pressure, however, also decreases overall film deposition rate and increases the chance of incorporation gases into the film.

In addition to the PLD system, a custom-built magnetron sputter system was also employed to deposit films. Figure 1.4 provides a schematic of this deposition tool. A typical sputtering tool consists of a vacuum chamber, which contains a substrate and at least one "gun." A gun consists of a target, ground shield and a power source to electrically bias the target. In this study, oxygen and argon were fed into the vacuum chamber. The power source is used to negatively bias the target, resulting in a strong electric field between the target and the ground shield. During operation, an Ar partial pressure of 3.5-30 mTorr is maintained to enable sputtering. Partial ionization of argon in the field between the target and ground shield results in the formation of a plasma. The Ar^+ ions in the plasma are accelerated by the electric field and impact the target with enough energy to "sputter" atoms from the target surface. These sputtered target

atoms then travel to and deposit onto the substrate. In the sputter system used in this study, a magnetron gun is used in which secondary electrons ejected from the target are magnetically confined to the region near the target. Collisions between these electrons and neutral argon atoms increases the plasma's degree of ionization, which increases the rate at which atoms are sputtered from the target. Two sputtering geometries were used in this study: off-axis and on-axis. In off-axis sputtering, the gun is positioned with its axis (normal to the target) parallel to the substrate. In on axis-sputtering, the gun is inverted so that the gun axis is normal to the substrate surface. In both cases, the substrate is rotated continuously to improve film uniformity. As with PLD, the inclusion of oxygen in the deposition atmosphere promotes full oxidation of the deposited film.

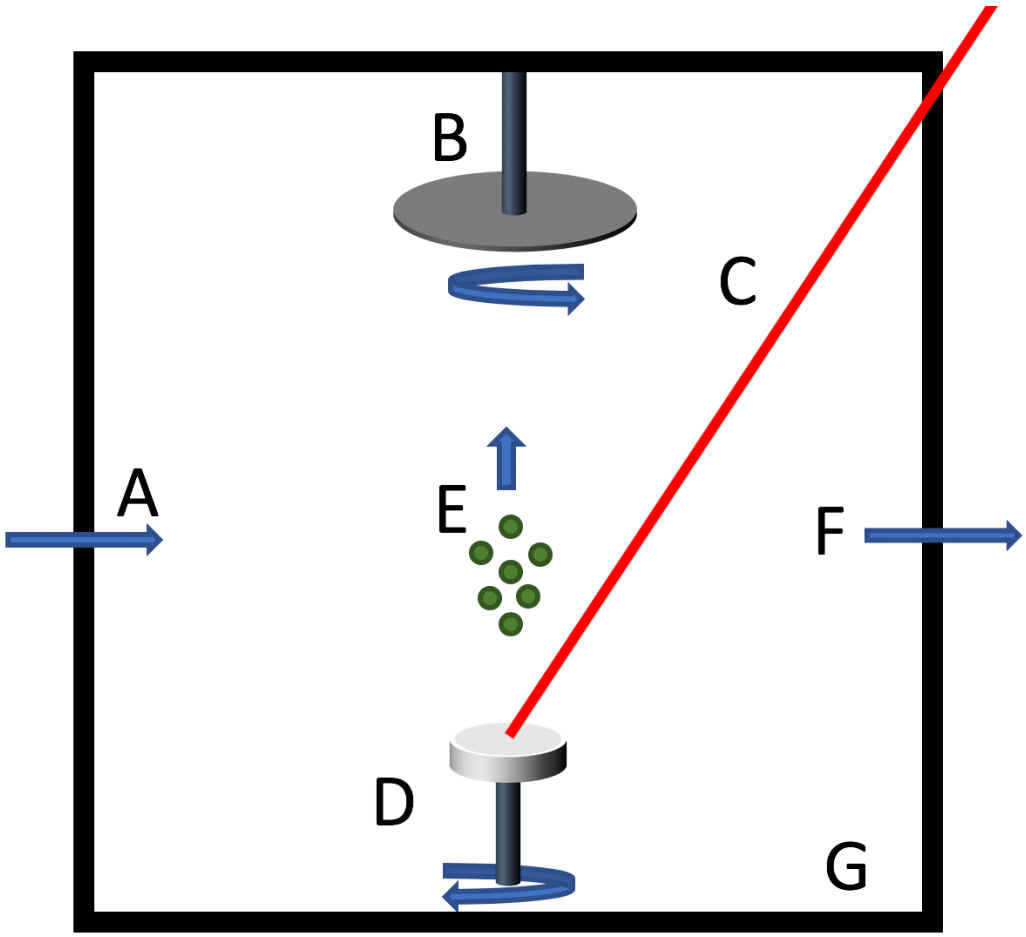

Figure 1.3: Schematic of PLD deposition system: (A) Ar/O_2 inflow valve (B) rotating substrate mount, (C) excimer pulse laser beam path, (D) rotating/rastering target holder, (E) ablated target material (F) exhaust to turbopump, (G) low pressure vacuum vessel wall.

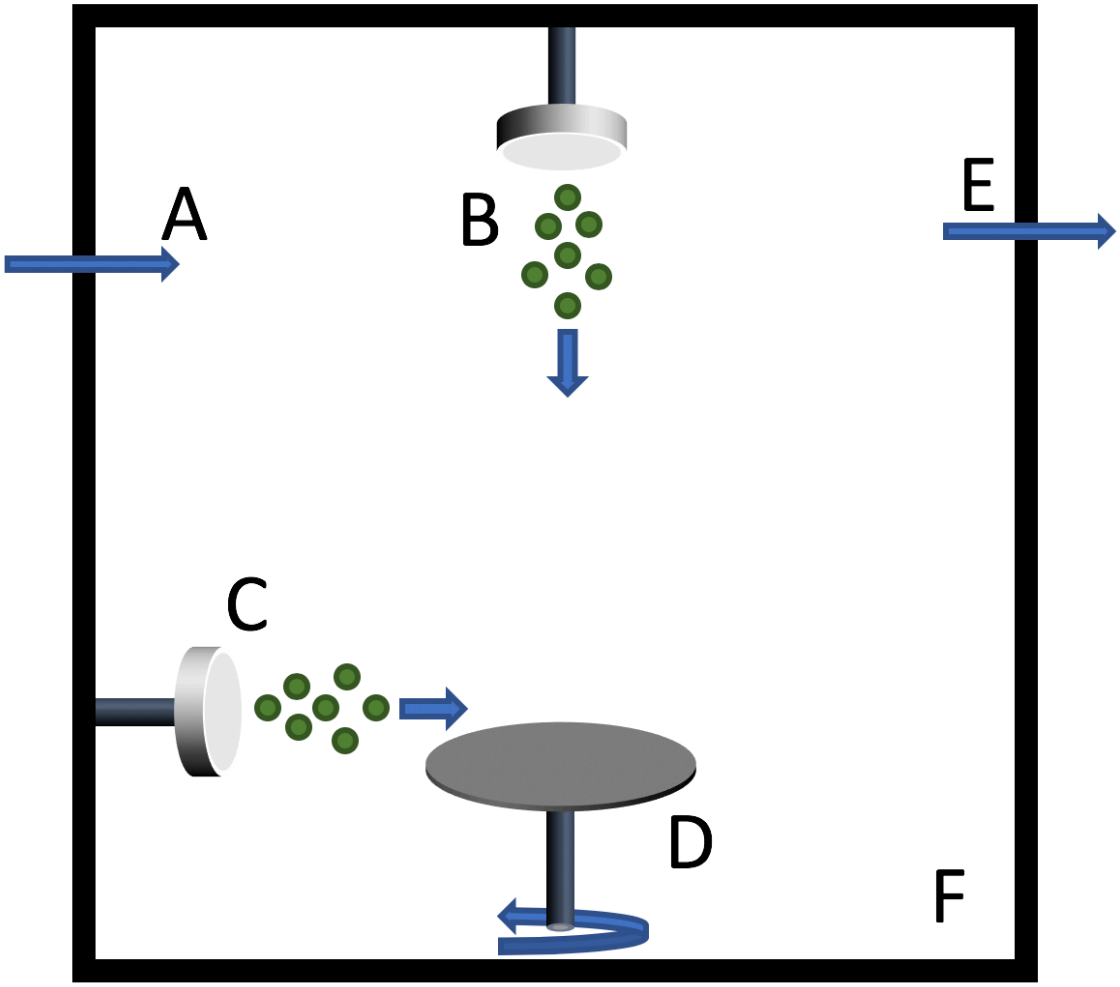

Figure 1.4: Diagram of sputter deposition system: (A) Ar/O_2 inlet, (B) on-axis sputter gun, (C) off-axis sputter gun, (D) rotating substrate holder, (E) exhaust to turbopump, (F) low pressure vessel wall.

2. Introduction to Laser Spike Annealing

In this study, thin films of barium titanate were thermally annealed using radiation from a 120 W, 10.6 µm wavelength carbon dioxide laser, in a process known as lateral gradient Laser Spike Anneal (lgLSA). Figure 1.5 provides a labeled photograph of the lgLSA setup. A carbon dioxide laser is used as a source for a beam of 10.6 µm radiation. The radiation is first passed through rotatable Brewster windows. By rotating the

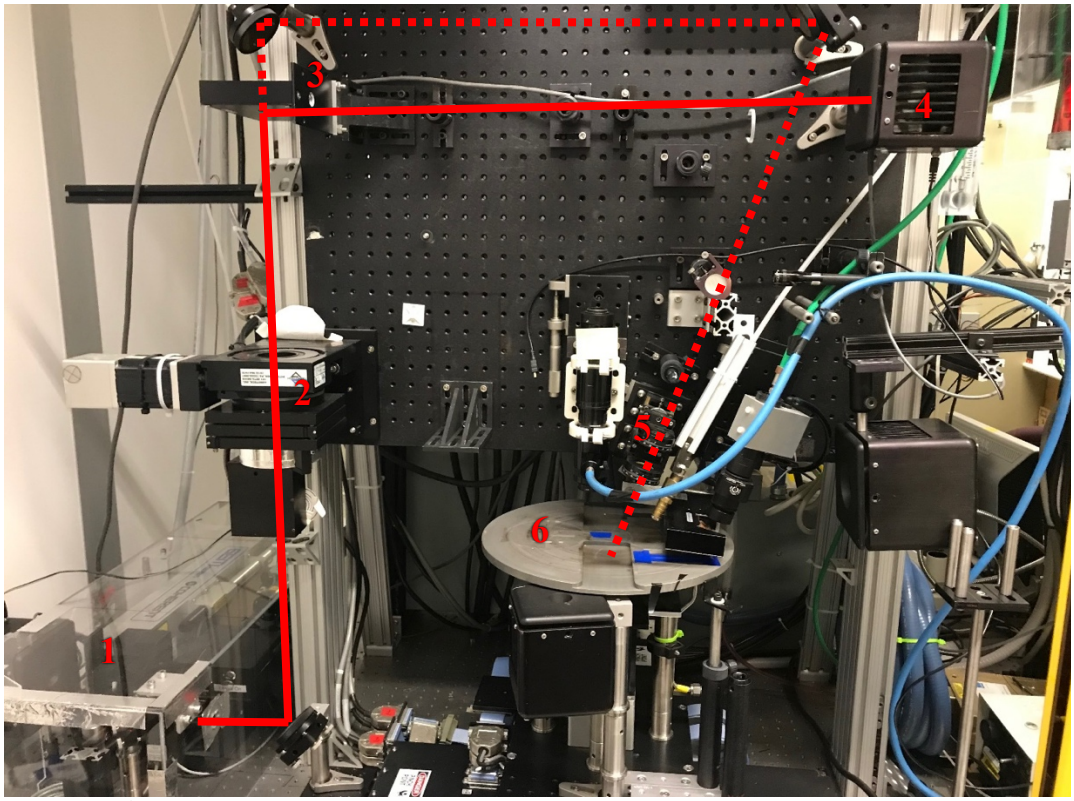

Figure 1.5: Labelled photograph of lgLSA experimental setup. The solid red line represents the laser beam path when the shutter is closed, whereas the dotted red line represents the laser beam path when the process shutter is opened. Labeled parts are as follows: (1) CO_2 enclosure, (2) CO_2 attenuator, (3) process shutter, (4) beam dump and power meter, (5) focusing optics, (6) sample stage.

Brewster windows relative to one another, the power of the transmitted radiation beam can be attenuated down from the power at the laser source. After attenuation, the laser

radiation transmits to a process shutter. When this shutter is closed, the radiation is diverted into a beam dump, where a thermocouple based power meter measures the transmitted laser power. When the shutter is opened, the beam is instead directed through a series of optical lenses. After passing through the optics, the beam irradiates the sample at an incident angle of 23° from vertical. The resultant footprint of the laser on the sample surface is a bivariate Gaussian with a major axis FWHM of 660 μm and minor axis FWHM of 90 μm. To cease the laser annealing, the shutter is closed again. The mechanism to open the shutter is actuated by a solenoid, whereas the shutting method is actuated by a spring. As a result, the shutter can open much quicker than it can close.

In the experimental setup, the sample was mounted to an X-Y stage. Using the stage to translate the sample relative to the laser allowed for different spots on the sample to be annealed without remounting the sample. Moreover, the setup allowed for the sample to be in motion during the anneal. By moving the stage at a constant velocity during an anneal, the dwell time of the anneal was controllable. In this study, the stage motion was set to be perpendicular to the major axis of the laser footprint during anneals.

Previous to this study, the laser annealing system was calibrated using a two method approach involving relative and absolute temperature measurements. For relative temperature calibration, photolithography was used to create several platinum resistors on a <100> oriented, 0.01-0.02 Ω-cm, p-doped Si wafer. The pattern of resistors allowed for temporally and spatially resolved resistance data to be collected during laser irradiation. Since the resistivity of platinum scales linearly with temperature, the temperature of each resistor relative to one another could be collected. For absolute

temperature calibration, rows of gold dots were deposited on a separate substrate with identical specifications to the first substrate. The sample was annealed with the path of the laser perpendicular to the rows of dots. Optical microscopy was then used to identify which dots were heated past the melting. The melted dots furthest from the laser path center indicate an area where the temperature was roughly equal to 1337 K. Therefore, the resistivity change measured at this distance from the laser center on the resistor sample was defined to equal 1337 K. From this reference point, spatially and temporally resolved absolute temperature data was obtained from the resistivity measurements. The results from these calibration runs show that the profile of peak temperature achieved during an anneal is a Gaussian centered about the center of the laser path. Isothermal contours of this Gaussian run parallel along the direction of the laser scan. Figure 4 displays the thermal profile of an lgLSA typical to this study.

The use of a carbon dioxide laser provides several advantages, but also results in some sample limitations. Firstly, the long wavelength of the laser radiation is significantly below the bandgap of barium titanate, preventing energy absorption through electron excitation. This allows the laser to travel through the barium titanate with minimal power loss. With the bulk of the laser energy reaching the substrate, the calibrations from the above described experiment remain accurate. However, the carbon dioxide laser energy is also well below the bandgap of Si and other conventional semiconducting substrates. Free electron absorption enabled by the p-type dopants allow appropriately doped Si substrates to effectively absorb 10.6 μm wavelength photons over a relatively short depth. A short laser absorption depth is critical for this study, since it results in the heating of a small volume of substrate . This small volume can be quenched by the

unheated substrate quickly through thermal conduction, allowing access to μs-ms scale quench times. Therefore, the substrates used for this study were all <100> oriented, 0.01-0.02 Ω-cm, p-type Si wafers.

3.Introduction to Synchrotron X-Ray Diffraction

In crystalline materials, long range atomic ordering forms a crystal lattice, which contains several sets of periodically spaced atomic planes. When EM radiation encounters an atomic plane, it can transmit through, scatter off or be absorbed. As depicted in Figure 1.6, when EM radiation scatters off different planes, the scattered rays may interfere with one another. Equation 1.1 gives the conditions for constructive interference in diffraction, where n is an integer, λ is the radiation wavelength, d is the spacing between atomic planes, and θ is the incidence angle of the radiation.

$$Equation\ 1.1:\ \cdot \lambda = 2d \cdot sin(\theta)$$

As implied by Equation 1.1, λ must be on the order of the separation between atomic planes. Thus, radiation with wavelengths on the order of ~1 Å are necessary for diffraction experiments, well within the x-ray spectrum. In a typical x-ray diffraction (XRD) experiment, a monochromatic x-ray source will be used, so that λ is a fixed, well defined quantity. θ is typically controlled as an experimental variable within XRD experiments. When measuring x-ray intensity as a function of diffraction angle, intensity peaks will exist around diffraction angles that satisfy Bragg's Law for the radiation wavelength and atomic plane spacings in the crystal. The location of these peaks can be compared with literature to determine the crystal structure of a material.

XRD can be used to determine much more than the microstructure of a crystal material. For example, by measuring the offset of x-ray peaks from values reported in the literature from annealed, strain-free samples, one can determine the stress state of a crystal material. The actual width of the peaks can be related to the average domain size of the crystals by the Scherrer Equation (Equation 1.2), where τ is the average domain size, K is a dimensionless shape factor approximately equal to 0.9, λ is the x-ray wavelength, β is the full width half maximum of the intensity peak, and θ is the angle of the diffraction peak.

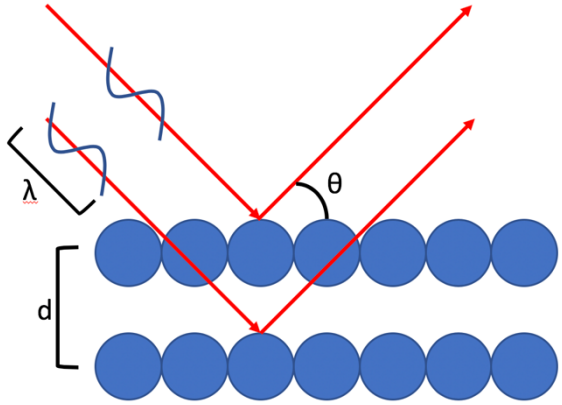

Figure 1.6: A schematic representation of Bragg diffraction in a crystalline material.

$$Equation\ 1.2: \tau = \frac{K\lambda}{\beta \cos(\theta)}$$

Typical laboratory XRD tools use a beam of high energy electrons to bombard a metallic target anode. The high energy electrons can excite inner shell electrons in the target. When the excited electrons return to their ground state, they release characteristic x-ray radiation suitable for use in XRD studies. However, this process is produces a great deal of waste heat. As a result, the rate at which a typical laboratory XRD tool can generate x-ray photons is limited by the ability for the tool to dissipate heat from the target. Another technique to generate x-rays for diffraction studies uses synchrotron radiation. In this study, the Cornell High Energy Synchrotron Source

(CHESS) was used as an x-ray source for XRD studies. CHESS uses a linear accelerator to accelerate charged particles (electrons and positrons) to energies on the order of a few hundred MeV. These excited particles are injected into a circular storage ring where they are further accelerated to 5 GeV. While the particles are confined in the circular, they are constantly accelerated to maintain a circular trajectory. The particles are then passed through an undulator, which stimulates the release of intense synchrotron radiation. When compared to typical laboratory anode x-ray sources, synchrotrons emit much higher x-ray intensities. In this study, complete diffraction patterns were captured from 30 ms of synchrotron x-ray exposure. A comparable measurement would take approximately 60 s in a typical laboratory XRD instrument. Without the rapid data acquisition enabled by a synchrotron x-ray source, the collection of the 125,000 individual diffraction patterns used in this study would have been time prohibitive.

4. Introduction to Optical Reflectometry

Optical Reflectometry is a powerful method that allows the characterization of the index of refraction and extinction coefficient of a thin film as a function of wavelength. The general principal of this technique involves irradiating a transparent thin film sample on a reflective substrate with a broad spectrum of light. When the light encounters the air-film interface, some light is reflected while the remainder is transmitted. Since the refractive index of the film is higher than the index in air, the phase of the light is shifted 180°. The transmitted light travels through the film to the substrate, where a majority is reflected. This reflection also shifts the phase of the light

by 180°. When the transmitted light returns to the film-air interface, it is often at a different phase than the reflected light. This phase difference is quantified by the optical path distance (OPD) of the transmitted light. The OPD for transmitted light at a 90° incident angle is given by Equation 1.3, where n_{film} is the index of refraction as a function of wavelength, and d_{film} is film thickness.

$$Equation\ 1.3: OPD = 2n_{film}(\lambda) \cdot d_{film}$$

When the OPD for a given wavelength of light is equal to a whole number multiple of that light's wavelength, the reflected and transmitted light will be perfectly in phase when leaving the sample surface. This results in a perceived increase in intensity of that wavelength of light reflecting off a sample. Conversely, if the OPD satisfies Equation 1.4 (where *n* is an integer and λ is the light wavelength in air), the reflected and transmitted light will be perfectly out of phase when leaving the sample surface. The resultant destructive interference decreases the perceived intensity of that wavelength of the light reflecting off the sample.

$$Equation\ 1.4: OPD = \left[n + \frac{1}{2}\right]\lambda$$

By measuring the intensity of light reflected off the sample as a function of wavelength, it is possible to quantify the OPD of the film. From this, it is possible to evaluate a film thickness, if one assumes a known index of refraction. Or conversely, if one assumes a film thickness, it is possible to solve for index of refraction. Different phases of a given material often have substantially different indices of refraction. Thus, monitoring a film for dramatic changes in refractive index also presents as a method to identify phase changes.

CHAPTER 2: EXPERIMENTAL PROCEDURE

Description of Laser Spike Annealing Experiment

In this study, the primary experimental variables were peak anneal temperature and dwell time. As previously described, the peak anneal temperature was controllable through the positioning of rotatable Brewster windows. By increasing the rotational offset between the two Brewster windows, the transmitted laser power can be attenuated. Based on previous calibration runs, the selected power range explored in this study was 22-60 W. From calibration experiments, these annealing conditions result in peak anneal temperatures from 600 °C to 1300 °C.

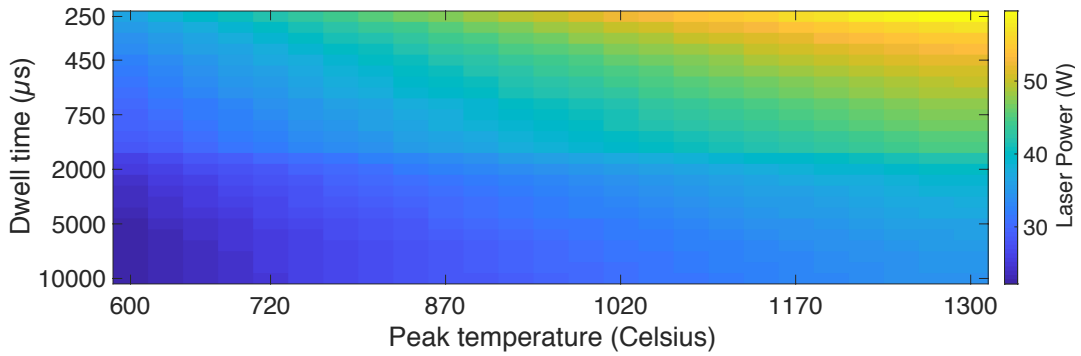

FIGURE 2.1: Heatmap relating anneal conditions (dwell time and peak temperature) to laser power output.

Additionally, the selected stage velocities were chosen to be in the range of 0.4 to 0.01 m/s, corresponding to 250 μs to 10 ms dwells, respectively. In this study, the dwell time is defined as the minor-axis FWHM of the laser footprint divided by the scan velocity. The peak quench rates achieved with these dwell times vary from 10^6 °C/s for 250 μs dwells to 10^4 °C/s for 10 ms dwells. The laser annealing process resulted in "stripes" of annealed film 5 mm in length. With the exception of the PLD-deposited sample, which was annealed with a more limited set of conditions, each sample contained 625 anneal stripes with unique peak temperature-dwell combinations. For samples subjected to the complete 625 stripe pattern, each stripe was separated by 2

mm lateral to the long dimension of the stripe. There was no separation between the stripes along the long dimension of the stripes. The temperature-dwell conditions between each stripe were randomized to reduce the chance of systematic error.

Physical Vapor Deposition of Barium Titanate Thin Films

For deposition rate calibration of PLD deposited films, 4" <100> Si substrates were first marked along a diameter with a sharpie marker. A substrate was then placed into the Neocera Ex200 system with a 2" diameter barium titanate target. The system was then pumped down to a base pressure of 10^{-5} Torr. The substrate and the target were both rotated at 20°/s, while the target was rastered over a distance of 2 inches, so that the laser would pulse over the entire target area during the deposition. At this point, any gases needed were fed into the chamber. A 1500 pulse ablation run at a 9 Hz pulse rate was carried out while the shutter was closed to clean the surface of the target. After the pre-deposition ablation was completed, the shutter was opened and laser pulsed the target 15,000 times at 9 Hz. After deposition, the wafer was doused in acetone and scrubbed with a cotton swab. This process dissolved the sharpie ink and liberated any film above it, exposing a channel to the wafer surface. Following this, the wafer was rinsed with IPA to remove any residual acetone, and blown dry with nitrogen. A KLA-Tencor P7 profilometer was then used to measure the height difference between the wafer surface and deposited film at several points extending from the radius. Additionally, the profilometer was used to characterize the roughness

TABLE 2.1: Parameters for explored PLD recipes

Recipe Name	Working Pressure (Torr)	Supplied gases (sscm)	Max Deposition rate (Å/pulse)	Ra roughness (nm)
A	10^{-5}	-	0.1522	4.6
B	10^{-2}	10 O_2	0.1375	1.3
C	10^{-2}	9 Ar 1 O_2	0.1215	2.8

of the film. This was accomplished by taking long line scans across a region of the film far from the lift off trench. Table 2.1 tabulates the conditions of the three tested recipes, as well as maximum deposition rates and film roughness. Figure 2.2 depicts a PLD sample with a liftoff trench used for profilometry thickness measurements.

For sputter deposition rate calibrations, a 4" <100> Si wafer was marked along a diameter with a streak of black wax. The wafer was then placed in the deposition chamber of the sputter system, and the chamber was pumped to a base pressure of 10^{-6} Torr. At this point, argon or oxygen (if called for in the recipe) was pumped into the chamber. Before all sputter depositions, the target was sputtered for several minutes while a shutter prevented deposition onto the substrate. This was performed to clean the surface of the target of any potential contaminants. Table 2.2 tabulates selected deposition parameters for the calibration runs. After deposition, the substrates were removed. A cotton swab doused with trichloroethylene was used to dissolve and scrub away the black wax, exposing a channel to the substrate. Acetone and IPA were then used to remove any remaining residue. The depth of the trench was measured with profilometry in an identical fashion to the PLD films.

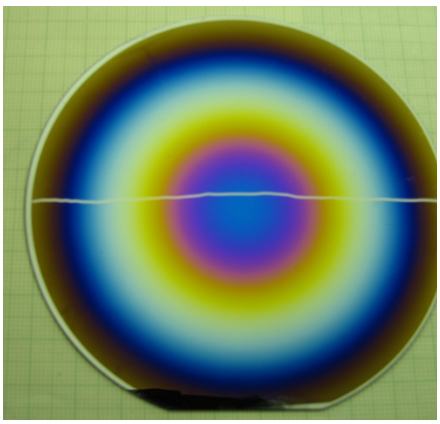

Figure 2.2: A PLD deposited $BaTiO_3$ sample with liftoff trench exposing underlying silicon wafer.

Table 2.2: Recipes used for sputtered films during study.

Material	Geometry	Working pressure (mTorr)	Power W	Atmosphere	Deposition rate (nm/min)
$BaTiO_3$	Off-axis	30	50 RF	90% Ar, 10% O_2	2.50
Ti	On-axis	3.5	20 DC	100% Ar	4.26

Following deposition rate calibrations, one PLD sample and three sputtered $BaTiO_3$ samples were prepared for laser spike annealing. Table 2.3 provides further details for the samples prepared for laser spike annealing.

TABLE 2.3: Details of samples prepared for laser spike annealing. All samples were deposited of <100> Si p-type wafers with resistivities of 0.01-0.02 Ω-cm.

Sample Name	Deposition method	Ti sticking layer nominal thickness (nm)	$BaTiO_3$ Thickness (nm)	Anneal dwell range (ms)	Anneal peak temperature range (°C)	Notes
18PLD1	PLD	-	73-243	150-10000	500-1200	Native etched from wafer before deposition
18F73	Off-axis Sputter	-	250-430	250-10000	600-1300	On native oxide
18F114	Off-axis Sputter	12	250-430	250-10000	600-1400	On native oxide
18F118	Off-axis Sputter	7	250-430	250-10000	600-1400	On native oxide

Description of WXRD setup

After annealing, sample 18F73 was selected for further analysis using WXRD at CHESS in the G3 hutch. In the hutch, a beam of 1.0972 Å x-rays was emitted from the synchrotron parallel to the ground. The sample was mounted to an X-Y stage, which was itself inclined 6° from the horizontal. Optics were used to focus the x-ray beam onto the sample. The resulting beam footprint was approximately 15 μm by 20 μm,

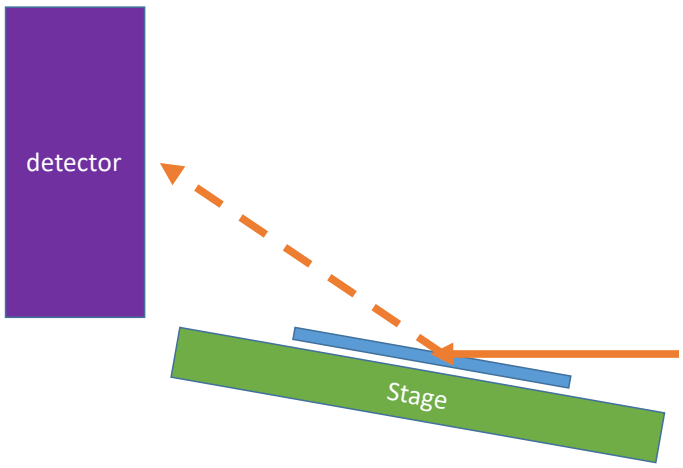

Figure 2.3: Schematic of WXRD setup. Incoming x-ray (solid orange) strikes the sample (solid blue) and diffracts (dashed orange) into the detector (solid purple).

with its long direction oriented parallel to the long dimension of the anneal stripes. A Dectris Pilatus 100k pixel array detector was mounted 92 mm horizontally behind the beam-sample irradiation point. The Pilatus 100k captured a 1030x1065 pixel grayscale images of x-ray intensity. Each image captured x-rays diffracted over the 2θ range of 22.25-45.65°. Figure 2.2 provides a schematic of the experimental x-ray set up. Spot-XRD measurements were taken at 202 locations at 10 µm intervals along a line perpendicular to the long dimension of each anneal stripe. This setup allowed spatially resolved diffraction data to be captured from each stripe at 10 µm resolution. Information regarding the calibration and correction of synchrotron data can be found in the appendix of this thesis.

Optical Reflectance Data Collection

In addition to synchrotron diffraction data collection, optical reflectance spectroscopy data were also collected for sample 18F73. In this experimental setup, the sample was mounted to an XY stage. Optics were used to focus a light source to a circular spot approximately 10 µm in diameter. A fiberoptic cable transmitted reflected light to a spectrometer, where wavelength-resolved intensity data was captured. Prior to any sample data collection, two calibration measurements were carried out. A dark current

measurement was first collected by taking a reading from the spectrometer while the fiberoptic cable was intentionally positioned over an “open” area with no sample; this collected scattered light within the system. Subsequently, a measurement was take on a highly reflective mirror, with >99% reflectivity over the optical band used in this experiment. Following calibration readings, the XY was stage was used to take successive point measurements at 10 μm intervals across anneal stripes in a similar manner to the synchrotron data collection.

Atomic Force Microscopy

An Asylum MFD3D Atomic Force Microscope was used to characterize the topography of the samples after laser spike anneals. For this experiment, annealed wafers were cleaved in samples approximately 7.5x7.5 millimeters. A Si cantilever and tip were used to characterize the surface in AC-air mode. When operating in AC air mode, the tip oscillated at its resonant frequency just above the sample surface. Changes in the surface topography were detected as deviations in the resonance frequency. Through this method, the surface topography of the sample could be analyzed with 0.5 Å vertical resolution. Since the tip never contacted the surface, contamination and damage to the sample was avoided.

CHAPTER 3: ANALYSIS AND DISCUSSION OF RESULTS

Comparison of Deposition Methods and Recipes

For PLD deposited $BaTiO_3$, all explored recipes had peak deposition rates in excess of 1 nm/s at the center of the film. Recipe A exhibited the highest peak deposition rate. This is likely attributable to the comparatively lower working pressure in recipe A over other recipes. In Recipe A atoms ablated from the target will undergo fewer collisions with vapors present in the deposition chamber. As a result, ablated atoms in lower pressure environments will deviate less from their original trajectory than ablated atoms in higher pressure environments. This results in film growth concentrating at the point on the wafer closest to the ablation point on the target. The increased frequency of collisions between ablated atoms and vapor in the deposition chamber associated with higher pressure depositions, conversely, results in more uniform film growth. As seen in Figure 3.1, the film thickness is reasonably uniform within a centimeter of the wafer center for all three recipes, but rapidly drops off towards the edge of the wafer. Overall film uniformity, measured by relative mean absolute difference, is tabulated in Table 3.1. Low relative absolute mean differences correspond to uniform films. These data support the notion that the low pressure of recipe C results in decreased film uniformity.

Table 3.1: Relative mean absolute difference for explored PLD recipes.

Recipe	A	B	C
Uniformity	38.75%	36.07%	33.5%

Also of note is the discrepancy between the uniformity in recipes B and C. Although both recipes were carried out at a working pressure of 10 mTorr, recipe C displayed noticeably better uniformity than recipe B. This may be explained by the difference in gas species present in the deposition atmosphere for the two recipes. As recipe B was a

pure O_2 atmosphere, the average gas particle molar mass was 32 g/mol. The atmosphere of recipe C was mostly 90% Ar and 10% O_2, with an average particle molar mass of 39 g/mol. It can be expected that ablated atoms travelling through an atmosphere of heavy particles undergo more scattering than when travelling through an atmosphere of less dense particles. This mechanism can explain the improved film uniformity of recipe C when compared to recipe B.

Figure 3.2 depicts the deposition profile resulting from an off-axis sputter deposition of barium titanate using the sputter system. As opposed to on-axis sputtering or PLD, the periphery of the wafer is geometrically closest to the target. This results in a deposition profile that resembles an inverse of a typical PLD deposition profile. The mean absolute deviation for the off-axis sputtered $BaTiO_3$ was measured to be 19.38%. The arithmetical mean deviation of film height, Ra, was used to quantify local film roughness. Profilometry of the off-axis sputtered $BaTiO_3$ measured an Ra value of 1.2 nm, which indicates a smooth film surface free of large vertical artifacts. Electron microprobe analysis was planned to be used to study the stoichiometry of the three PLD recipes and the sputter recipe. However, inconsistent results followed by the decommissioning of the electron microprobe tool made detailed stoichiometric information unavailable for this study. Alternative elemental composition analysis methods available (namely EDS and XPS) were not expected to yield accurate enough data for meaningful analysis. However, given the extensive use

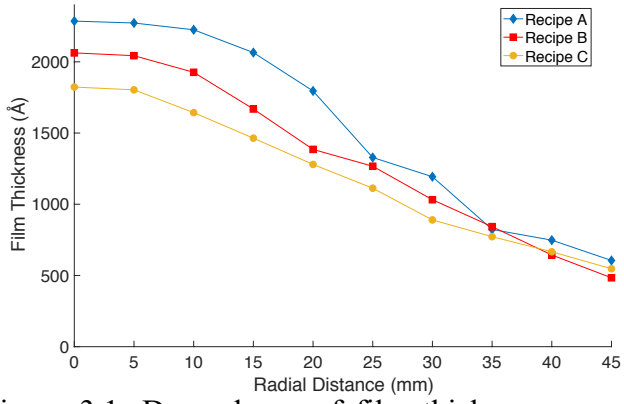

Figure 3.1: Dependence of film thickness on radial distance from wafer center for PLD deposited $BaTiO_3$ samples.

of RF sputtering to deposit BaTiO3 in literature, it was assumed that sputtering produces reasonably stoichiometric films.

From the results of profilometry analysis, off-axis sputtering was selected as the primary deposition method for this study. Off-axis sputtering produced films with almost twice the uniformity of the best PLD recipe, with a relative mean absolute difference of 18.7%. Additionally, the off-axis sputtered films possess a region of exceptional uniformity extending from the center of the wafer to approximately 2.5 cm radially outward. Another advantage of sputtering over PLD is film smoothness. Although the smoothest PLD film and the sputtered film possess similar Ra values, PLD is notorious for its production of "boulders." While the PLD ablation plume is generally assumed to be composed of individual atoms, it routinely is found to contain larger particles on the order of several nm in diameter, which can deposit on the sample surface. The large area of the probe used in profilometry is ill-suited to detect small features such as boulders, and thus the Ra measurements for PLD deposited films may be inaccurate. Sputtering does not typically produce boulders, so the profilometry-measured Ra figure bears more credibility than the Ra figure for PLD recipes.

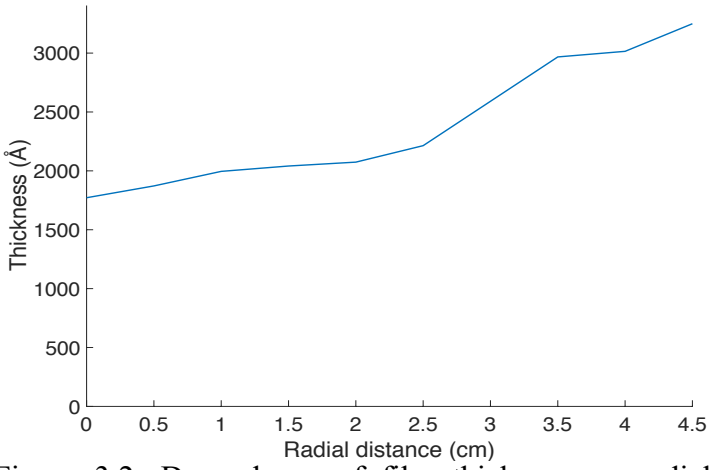

Figure 3.2: Dependence of film thickness on radial distance from wafer center for off-axis sputtered $BaTiO_3$.

Another advantage of sputtering over PLD is flexibility in target material. Although both methods are well-suited to the deposition of metal oxide materials like $BaTiO_3$, PLD struggles to deposit metals. The high reflectance of metals results in a significant

portion of the laser energy being lost to reflection, leading to slow film growth. For later samples in this study, a Ti sticking layer was sputtered immediately before $BaTiO_3$ deposition to enhance film adhesion. Such a sticking layer would not be possible to complete in a PLD tool. Sputtering a Ti sticking layer and then using PLD to deposit $BaTiO_3$ could be used to overcome this shortcoming, but that process would involve exposing the sample to atmosphere between depositions. Atmospheric exposure could lead to significant sample contamination, and would oxidize the Ti sticking layer. The multiple guns in the sputter system allowed multiple materials to be sputtered on a sample without breaking vacuum.

Optical Microscopy of Stripes

Optical microscopy of the annealed samples proved to be a quick, cost effective method of analysis for laser spike annealed samples. For many anneal conditions, optical changes to the film were observed to resemble stripes that follow the path of the anneal laser. Typical path widths were on the order of a few hundred μm. Features of this size are readily visible through optical microscopy, so more advanced imaging techniques were not required. Additionally, optical microscopy can also reveal changes to the optical thickness of a film, unlike electron-based microscopy techniques that may provide better magnification.

Figure 3.3 demonstrates several anneal stripes at different temperatures for identical dwells for sample 18PLD1. Optical microscopy of sample 18PLD1 did not indicate any damage to the film and the surface of all annealed regions remained specular. The tapered profile evident in figures 3.3B-D is attributable to the closing mechanism of the process shutter in the laser spike anneal setup. While the shutter opens rapidly with a

solenoid, the closing mechanism of the shutter is actuated by a much slower spring. This results in a slowly diminishing beam intensity at the end of each stripe.

For anneals with peak temperatures above 1000 °C and dwells longer than 1 ms, several dramatic, abrupt color transitions were observable through white light microscopy. The symmetry of the color transitions about the central long axis of the anneal stripe indicate that the mechanism leading to the color transitions is directly related to anneal temperature reached in the film. The first interpretation of the color changes was that the laser was ablating the film, and film thickness changes were to blame for the interesting optical behavior. However, the color transitions do not correspond to a thinning of the optical thickness of the film.

The next interpretation was that each color corresponded to a phase of $BaTiO_3$ with a distinct index of refraction. This interpretation would be most promising, as it would indicate the stabilization of five different phases of $BaTiO_3$. However, it was soon realized that the color sequence could correspond to a monotonic decrease in optical thickness as distance from the stripe center increases. The jump from red to violet most likely indicates a transition from first to second order interference fringes. Since the color transitions only occurred for longer dwells, their appearance is attributed to reaction at the film-substrate interface. Experiments show that $BaTiO_3$ on bare Si begins reacting at 800 ℃ to form barium titanium silicate during 20 minute anneals [23]. As sample 18PLD1 had its native oxide layer etched away, no diffusion barrier existed between the $BaTiO_3$ film and the Si substrate. Diffusion at the interface would enable the formation of a transparent silicate, which would increase the apparent optical thickness of the film. Since diffusion is a kinetic process, the depth of the silicate layer

would grow over time as mass diffuses across the interface. Moreover, since diffusivity increases with temperature, the silicate layer would be thickest at the hottest points on an anneal stripe. The lack of distinct color changes for anneals at shorter dwells, and the apparent increased optical thickness at center of anneal stripes strongly support this conclusion. Moreover, the onset of silicate formation at 800 °C, evidenced by the color changes in Figure 3.3B, strongly agree with findings reported in literature. The color change for the 600 °C peak temperature is not consistent with an increase in optical thickness. Additionally literature findings suggest that $BaTiO_3$ is stable against silicon at this temperature. As a result, this color change is believed to be attributable to densification and not reaction with the substrate.

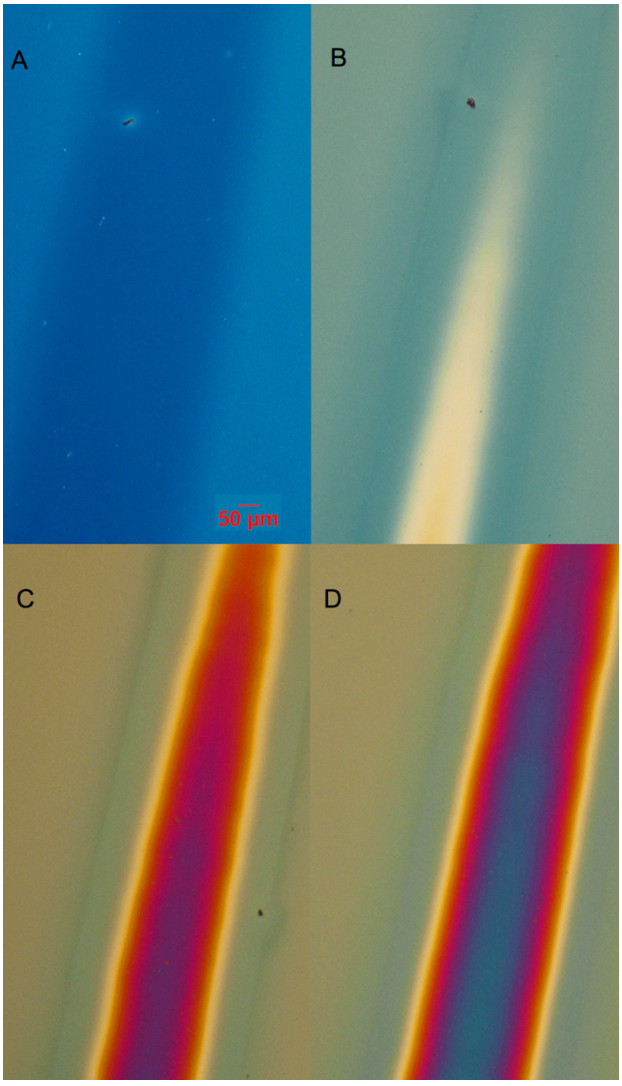

Figure 3.3: Images of 10 ms anneal stripes on sample 18PLD1 for different peak temperatures: (A) 600 °C (B) 800 °C (C) 1000 °C (D) 1200 °C. The scale bar provided corresponds to all sub figures. The laser moved from the bottom to the top of all images.

The intention of etching the oxide layer from the wafer before deposition of on sample

18PLD1 was to eliminate any parasitic capacitance that may occur on the film for future dielectric measurements. Given the ubiquitous use of $BaTiO_3$ as a dielectric material, a primary goal of this study was to characterize the effects of laser spike annealing processes on the dielectric constant of $BaTiO_3$. For these measurements, the fabrication of micro-capacitors was planned. These capacitors would consist of a patterned aluminum top electrode, an annealed $BaTiO_3$ dielectric layer and a highly doped Si bottom electrode. By measuring the capacitance of such a device, the dielectric constant of the laser spike annealed $BaTiO_3$ could be calculated. However, the existence of a native oxide layer between the $BaTiO_3$ and the substrate would effectively add a second capacitor in series to the experimental setup. This second capacitor would lower the measured capacitance, and suggest artificially low dielectric constants for the annealed $BaTiO_3$. Etching away the oxide would eliminate this source of error. However, the silicate that formed in 18PLD1 would likely be even more deleterious to dielectric measurements than the native oxide. As a result, all samples prepared after 18PLD1 had their native oxides left intact. Plans were made to thermally oxidize wafers to achieve a uniform oxide thickness of 20 nm before $BaTiO_3$ deposition to prevent diffusion and silicate formation. Since the thickness of this interface layer would be known to a high degree of certainty, capacitance measurements could be compensated for the effects of the oxide layer.

Optical micrographs of sample 18F73 presented starkly contrasting behavior to 18PLD1. For anneals with peak temperatures under 780 °C, the anneal either produced no visible change, or a slight color change. Figure 3.4 provides a micrograph of an anneal stripe on sample 18F73 exhibiting slight color change. For anneals above 780

°C, the $BaTiO_3$ film typically suffered extensive damage. Generally, the surface of all damaged film regions became rough and nonuniform. Profilometry performed on damaged areas revealed a jagged topography, with peak heights in excess of 1 μm above the film surface. Minima in the profilometry indicate that the film had been completely removed in some areas. Moreover, it was routinely impossible to keep all portions of a damage area in focus simultaneously during optical microscopy, evidencing the massive height deviations throughout the film.

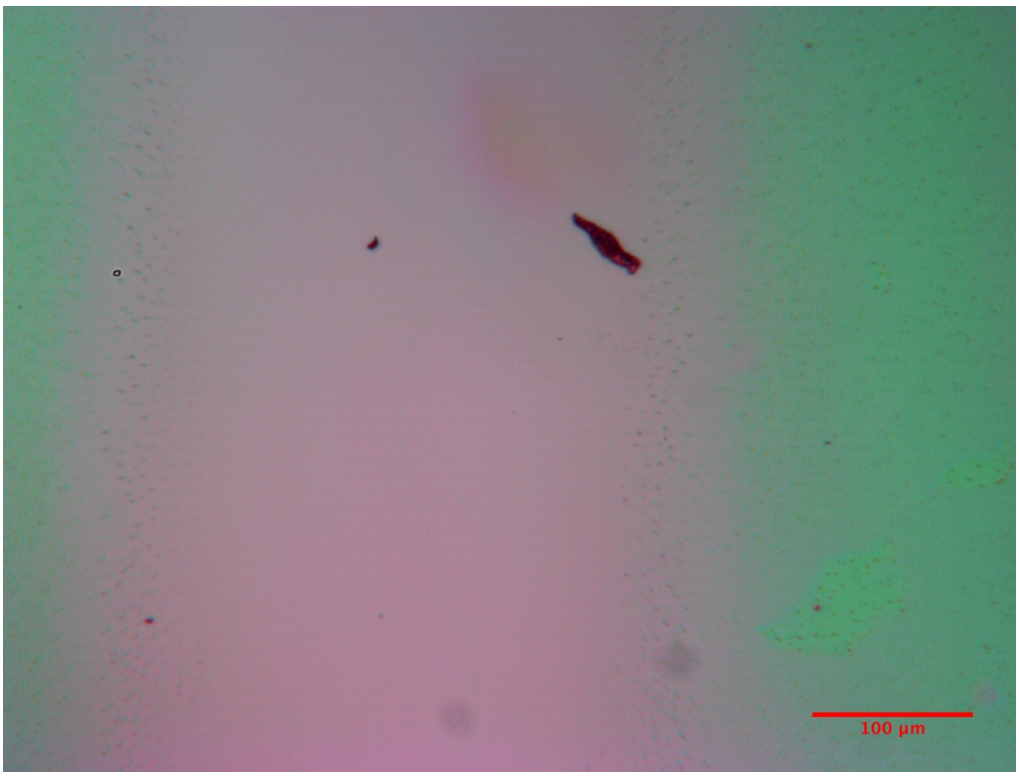

Figure 3.4: Image of area on sample 18F73 subjected to 780 °C anneal for 300 μs.

The color changes on 18F73 as depicted in Figure 3.4 are not attributable to silicate formation. Firstly, color changes are noted to occur at anneals below the 800 °C silicate formation threshold suggested by literature. Additionally, many anneals below 1 ms on 18F73 exhibited color changes. Since no HF etch was carried out on 18F73 before film

deposition, a thin SiO_2 layer exists between the wafer and the $BaTiO_3$. This layer inhibits diffusion between the film and the substrate and slows silicate formation. Anneals under 1 ms on 18PLD1 did not demonstrate silicate formation, despite the sample lacking an SiO_2 diffusion barrier. Therefore, the color changes on 18F73 in Figure 3.4 are not consistent with silicate formation.

Optical micrographs of anneals that produced damage to the film suggest a damage threshold of 780 °C. Films with peak temperatures beneath this did not exhibit damage. However, some anneal stripes with peak temperatures as high as 840 °C did not exhibit damage. Damage was noted to present in two dominant forms. Figure 3.5 provides a micrograph of damage produced by anneals with dwells of 1.5 ms and longer. These damage regions are characterized by extensive cracking and distinct regions of

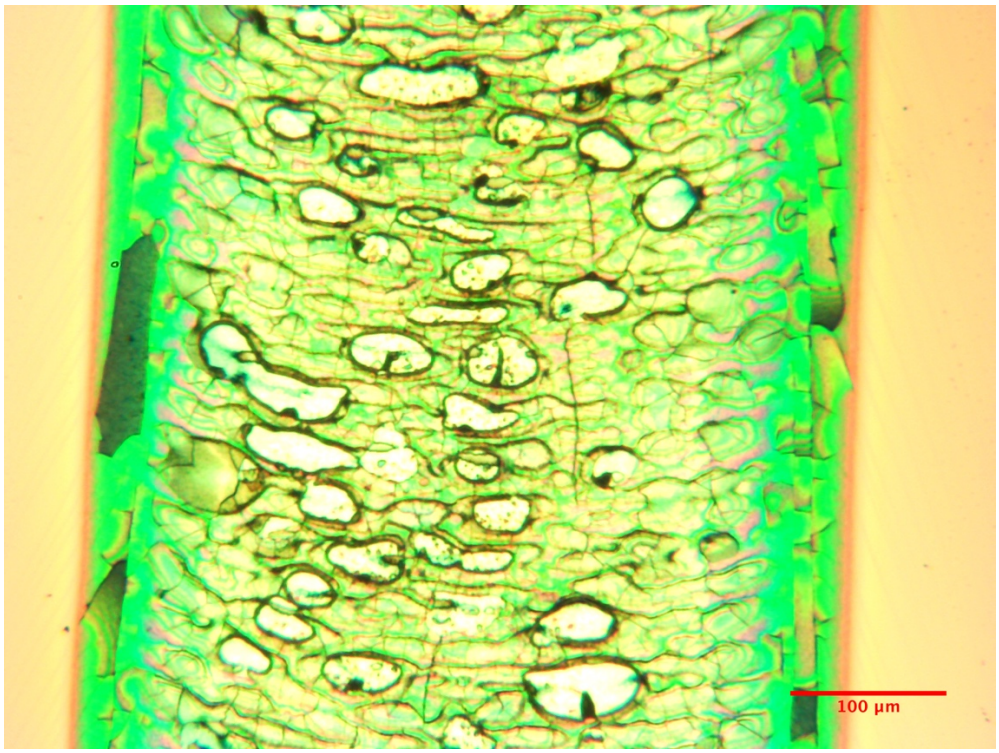

Figure 3.5: Image of area on sample 18F73 subjected to 1200 °C anneal for 2500 μs. During the anneal, the laser passed from the bottom of the image to the top.

inhomogeneous size. Striations also extend from the edge of the damage region. The striations are likely cracks that begin at the periphery of the damage area and then extend outward and against the laser scan direction. At the periphery of the damage area, the films color shifts. This behavior is reminiscent of the color change observed on anneals that do not exhibit damage. The film in this area appears uniform, specular and crack free. Moving closer to the center of the anneal stripe, the film again changes color. However, the film in this area is highly cracked. Moreover, chips and fragments of the film seem to be missing, with the underlying substrate occasionally observable. In the central region of the anneal stripe, the film surface appears to be comprised of irregularly sized and shaped scales. The region also has extensive cracking. Several of these cracks seem to follow a curved contour, which coincides with the retreating side of the laser profile. A likely explanation for this sort of damage is that the laser induced a melt in the $BaTiO_3$ film. The longer dwell associated with this melt allowed pools of molten $BaTiO_3$ to coalesce, resulting in the appearance of scales. As the laser moved off of the molten $BaTiO_3$, a solidification front followed, resulting in the contours of the temperature profile of the laser. Strain associated with solidification and the thermal gradient is believed to have caused the cracking. As the regions showing complete delamination are along the peripheries of the damage region, it is likely that the films in this area delaminated without melting. It should be mentioned that these films did not evidence any color changes indicative of silicate formation, suggesting that the native oxide layer was sufficient to prevent extensive interfacial diffusion.

Figure 3.6 provides a micrograph of damage characteristic for damaged films annealed less than 1.5 ms. These films exhibited dramatic surface roughening and darkening. On

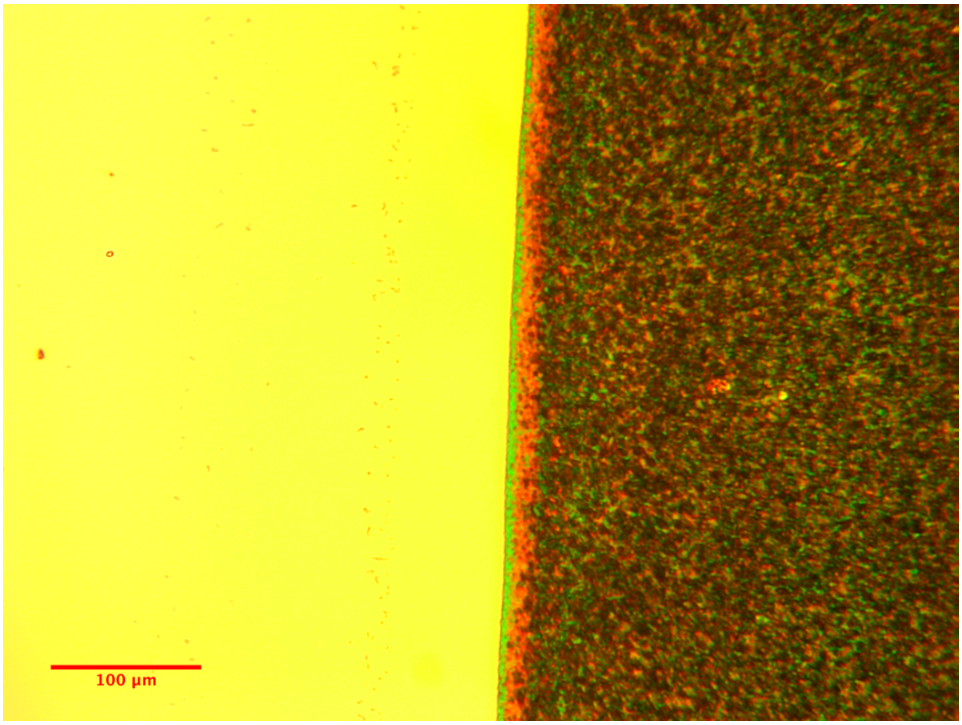

Figure 3.6: Image of area on sample 18F73 subjected to 1300 °C anneal for 750 μs. During the anneal, the laser passed from the bottom of the image to the top, with the anneal running along the right edge of the image..

the extreme peripheries of the stripes, color changes are observable. However, the order of these changes does not suggest silicate formation. Within these color change regions, a small number of dark grains are observable. Moving towards the center of the stripe, the density of the grains sharply increases. The underlying substrate is not observable on these stripes, suggesting that the film did not completely detach from the substrate and flake off. Profilometry of this stripe revealed a rough topography, with peaks up to 800 nm above the film surface. However, the profilometer did not identify any regions lower than the outlying film, again indicating that the film remained attached to the substrate after the anneal. As damage region shows no texturing consistent with the laser scan direction, it is believed that the film melted and then solidified. The brevity of the anneal duration did not allow molten regions to coalesce. Moreover, the stage motion

was likely too quick for a cohesive solidification front to occur, resulting in randomly distributed grains in the melt region.

A question raised by the results of the optical microscopy on 18F73 is the origin of the melt damage. Anneals on 18F73 were intended to have a maximum temperature of 1300 ℃, far below the melting temperature of 1600 ℃ for $BaTiO_3$. In order to better understand the nature of the damage, samples 18F114 and 18F118 were prepared and annealed. These two wafers included thin Ti sticking layers deposited between the Si and $BaTiO_3$. Additionally, they were subjected to anneals with peak temperature ranges from 600-1400 ℃. The Ti sticking layer was intended to increase cohesion of the $BaTiO_3$ to the Si substrate. In all other aspects, these samples were identical to 18F73. Analysis of 18F114 through optical microscopy did not reveal any changes to the film in annealed areas. This is attributable to the thickness of the Ti sticking layer. At 12 nm, the Ti likely reflected a significant amount of laser energy out of the film. This would significantly reduce the amount of laser energy deposited into the Si, and thus drastically decrease the peak temperature achieved in the film. Although the intended anneal profile was not achievable on this sample, it did demonstrate that the damage on 18F73 was not attributable to interaction between the $BaTiO_3$ and the laser alone. On this sample the laser transmitted through the $BaTiO_3$, reflected off the Ti, and travelled through the $BaTiO_3$ without producing visible changes to the film. This indicates that, as expected, the laser can pass through the $BaTiO_3$ with minimal losses to absorption.

Sample 18F118 was prepared and annealed identically to 18F114. However, the thickness of the Ti sticking layer was roughly halved. Optical microscopy of the sample post anneal demonstrated minor visible changed to the film. Although the Ti sticking

layer on this sample would reflect back some laser power, and thus reduce the peak temperature achieved, the layer was thin enough to allow enough transmission to significantly heat the substrate. Some damage was evident on the longest and hottest anneals. Figure 3.7 provides a micrograph of damage on 18F118. The cracks seen in this figure are consistent with compressive failure of the film. Unlike tensile failure, compressive failure results in delamination of the film from the substrate.

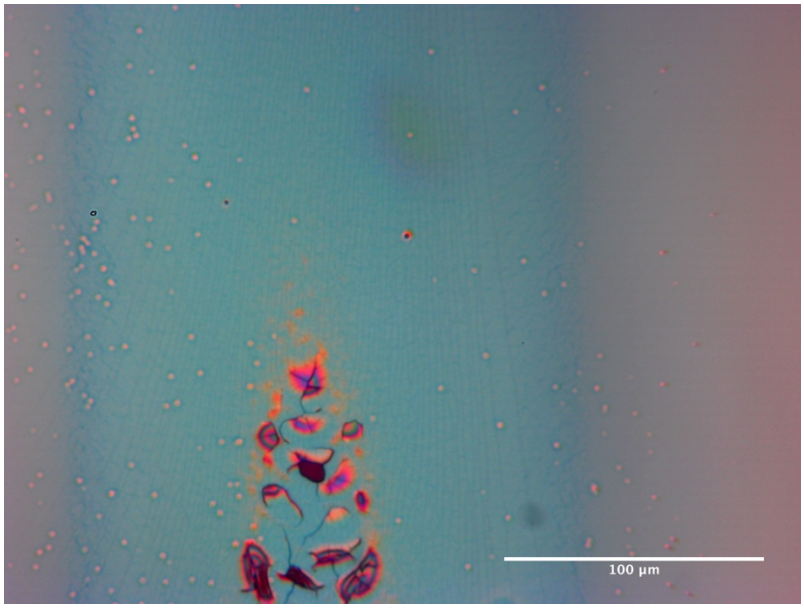

Figure 3.7: Micrograph of 1250 °C anneal for 8 ms on sample 18F118. The laser travelled from bottom to top during the anneal.

It is therefore likely that the damage in 18F73 was also instigated by compressive failure. As the sample was heated by the laser, the $BaTiO_3$ and the Si expanded. The thermal expansion coefficient for Si is roughly 2-4 times smaller than the coefficient for most metal oxides. Therefore, the mismatch in expansion would cause a compressive stress in the $BaTiO_3$ thin film. However, as previously mentioned, amorphous $BaTiO_3$ undergoes a 10% volume expansion before crystallization. This expansion would compound the thermal expansion coefficient mismatch stress, and lead to an even more compressively stressed film. Eventually, the film delaminates and buckles upward to accommodate the compressive stress. When this delamination occurs, the film loses

contact with the substrate, and conductive heat exchange can no longer occurs. As the absorptivity of $BaTiO_3$ for 10.6 μm light is low, but nonzero, the film would continue to heat up after delamination. If the film were in contact with the substrate, any difference in temperature between the substrate and film would quickly be equilibrated through thermal conduction. However, a delaminated film could continue to rapidly heat to melt, even if the underlying substrate was much cooler. This mechanism explains the apparent onset of melt damage seen in 18F73 for anneals far below that actual melting temperature of the film. As damage is intrinsically linked with delamination, the actual temperature threshold is difficult to define. Many uncontrolled factors, such as contaminants or defects on the wafer, could play a role in film delamination. As a result, there exists a lower limit to damage occurring, 780 °C, although some films were able to exceed this temperature without becoming damaged. It should be noted that the primary implication of this finding is that the temperature profiles achieved on 18F73 are far from the profile suggested by previous calibrations. The calibration profile should be considered as a lower baseline for actual temperature achieved on stripes exhibiting damage. However, the profile suggested by calibration can still be considered as a valid model for stripes not exhibiting damage.

Analysis of Optical Reflectance Data

Optical reflectance data was collected to gain insight to the optical properties of the film across an anneal stripe. As the data collection could be automated for an entire wafer, its implementation enabled rapid analysis of entire samples. As previously discussed, the annealing of sample 18PLD1 resulted in reaction between the $BaTiO_3$ and the Si substrate, resulting in the formation of a transparent silicate layer. This transparent silicate layer will influence the results of the optical reflectance data in unwanted ways. As a result, 18PLD1 was excluded from this sort of data collection. Additionally, samples 18F114 and 18F118 were not considered suitable for this study. The presence of the Ti sticking layer on these samples was observed to severely diminish the amount of energy the CO_2 layer could deposit in the substrate. Thus, the actual heating profile achieved is unknown for all stripes on the two samples. 18F73, which had no observable silicate formation nor a Ti sticking layer, was thus the only sample considered suitable for reflectance data analysis. Although the damage regions on this sample deviate from the expected heating profile, there exist ample area that is undamaged. It is from these areas that useful reflectometry data can be gathered

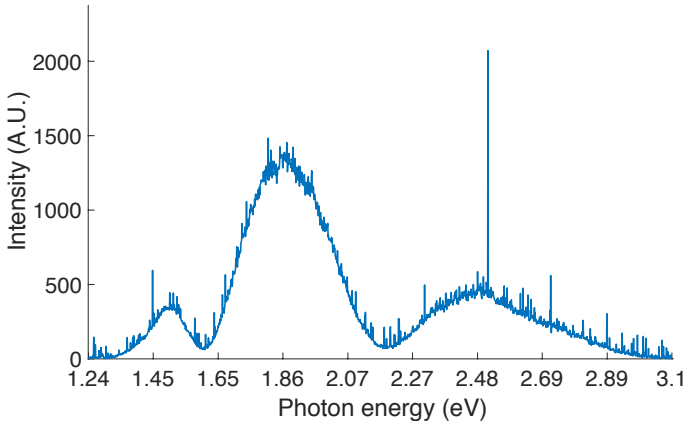

Figure 3.8: A plot of photon energy versus intensity for a reflectance spectrum collected at the center of a 450 μs 660 °C anneal stripe.

Figure 3.8 demonstrates raw data collected at a single unannealed point on 18F73. The raw data was normalized, background subtracted and smoothed. Following

normalization, 62,500 individual reflectance spectra were combined into heatmaps, an example of which is provided in Figure 3.9. These heatmaps were extraordinarily useful in spatially relating the effects of the laser spike anneals on the optical properties of the thin films. Moreover, it allowed the data to be condensed into 625 unique heatmaps, which allowed for rapid data analysis.

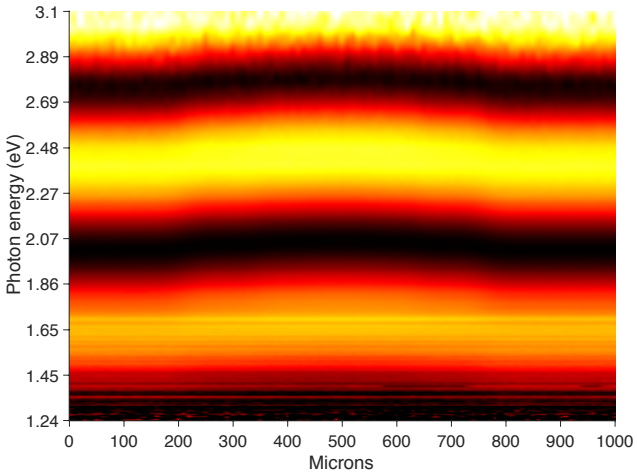

Figure 3.9: An optical reflectance heatmap across a 780 °C anneal 300 μs long.

Figure 3.9 represents a heatmap characteristic for a stripe that did not exhibit damage under optical microscopy. In these heatmaps, the vertical axis corresponds to photon energy and the horizontal axis corresponds to position on the wafer. Constructive interference fringes present as continuous yellow bands running horizontally across the image, while destructive fringes present as black bands running horizontally across the image. Towards the lateral center of the heat map, there is a slight bending upwards of the interference fringes. This change corresponds to a decrease in optical thickness of the film. This data is in excellent agreement with micrographs of undamaged stripes on 18F73, which also suggested an optical thinning of the film. As silicate formation would result in the opposite behavior, the optical reflectance data lends even greater confidence to the efficacy of the native oxide layer as a diffusion barrier. Additionally, the uniformity of intensity across the fringes suggest that the film surface was not roughened by the anneal and maintained a specular surface.

Figure 3.10 provides a heatmap for a damaged stripe annealed for 250 µs. As with undamaged stripes, the optical reflectance data suggests a slight decrease in optical thickness towards the center of the stripe. However, as distance to the center of the stripe decreases, the intensity of the signal at all wavelengths sharply decreases. This behavior is consistent with a roughening of the film surface, causing nonspecular reflection of light. This interpretation is supported by microscopy and profilometry of stripes annealed above 780 ℃ and shorter than 1.5 ms, which show surfaces too rough to produce specular reflections.

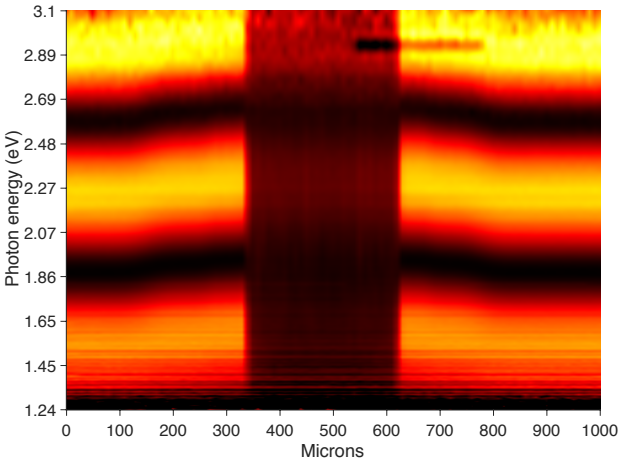

Figure 3.10: An optical reflectance heatmap across a 1300 °C anneal 250 μs long.

Figure 3.11 provides a heatmap for a damaged stripe annealed longer than 1.5 ms. As with the two previously discussed heatmaps, the optical thickness of the film evidently decreases towards the center of the anneal stripe. As with other damaged stripes, a dramatic change in reflectance data occurs at the onset of damage. However, in contrast to heatmaps similar to Figure 3.10, the damage in heatmaps for anneals longer than 1.5 ms is not characterized by a uniform loss in signal intensity. Rather the signal appears much noisier, with isolated regions of high intensity signal. It is likely that the film in this damage region is highly non uniform, although still somewhat specular. As

such, minima and maxima in intensity can still be made out in the heatmap, but they lack the consistency and symmetry of the undamaged stripes. Therefore, the abrupt change in behavior is believed to be primarily attributable to film damage, and not from the onset of different phases. This result is consistent with the previous discussion of microscopy for damaged stripes subjected to anneals over 1.5 ms.

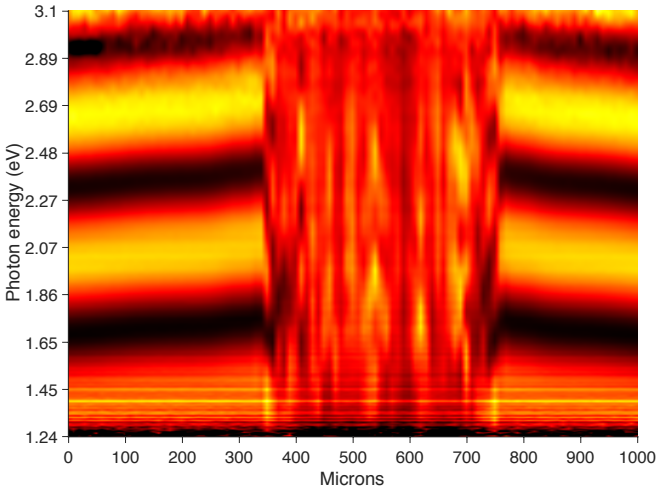

Figure 3.11: An optical reflectance heatmap across a 1200 °C anneal 2500 μs long.

The distinctive nature of damage in anneal stripes in reflectometry heatmaps proved to make reflectometry an efficient way to visualize damage on the wafer. Figure 3.12 provides a grid of reflectometry heatmaps on the sample 18F73. From this grid, the onset of damage is noted to occur at and above 780 ℃. However, the onset of damage varies considerably with anneal time, following no apparent trends. Notably, at the 750 µs dwell range, damage is apparent at 780 ℃, then not apparent at 810 ℃, and apparent again at and above 840 ℃. Also apparent is a stark change in damage behavior beginning at the 1.5 ms dwells. As suggested by the discussion of Figure 3.10 and Figure 3.11, at 1.5 ms the damage behavior shifts from signals characteristic of non-specular reflections to signals characteristic of specular reflections from a nonuniform surface. Another point of interest from the reflectometry grid is the apparent thickness dependence on optical thinning behavior. For heatmaps containing three reflectance maxima and showing no damage, as characterized by Figure 3.4, the interference fringes

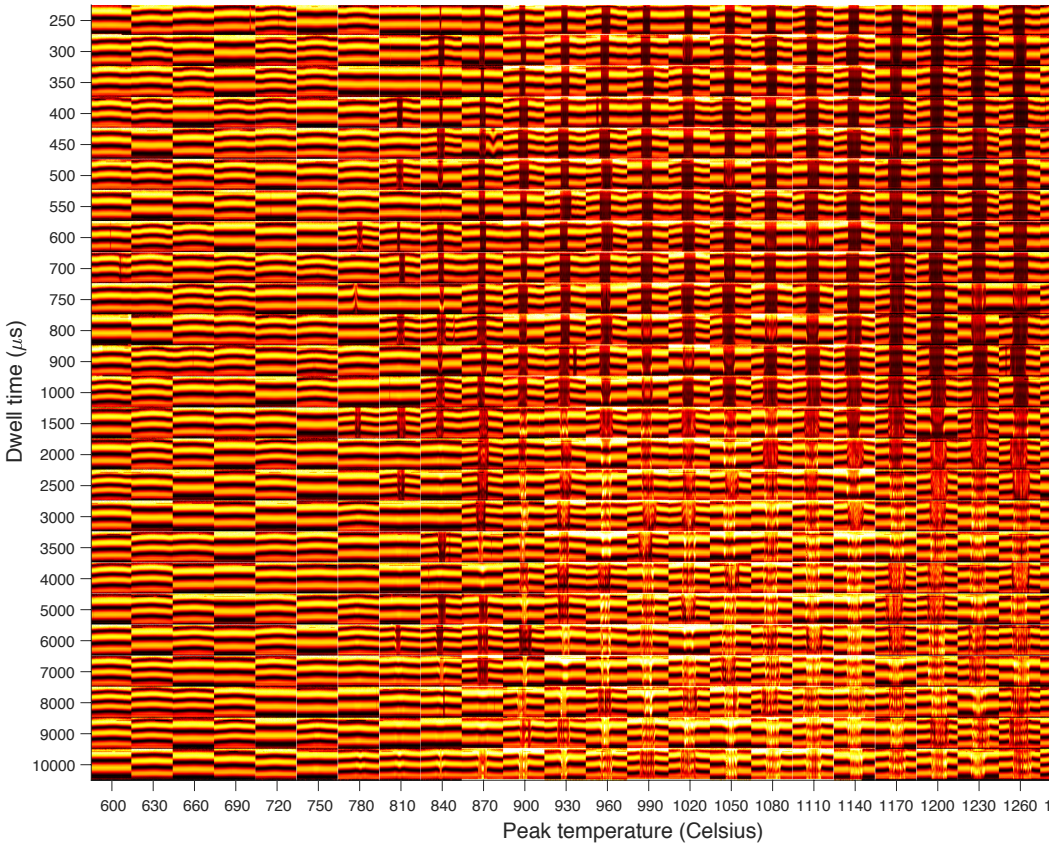

Figure 3.12: A grid collage of reflectometry heatmaps arranged by peak anneal temperature and dwell time.

bend upward towards the center of the anneal. However, this behavior is absent on heatmaps which contain only two interference fringes and show no damage. As heatmaps with fewer fringes are collected from thinner film areas, this behavior suggests that fringe bending has a dependence on film thickness. Due to the rotation employed during the off-axis film deposition, areas near the wafer edge alternate between periods of high deposition rate when they are closest to the target, and low deposition rate when they are furthest from the target. When the film is closest to the target, the sputtered atoms impinge on the substrate with the greatest velocity, a significant component of which is angled parallel to the substrate. This could result in “shadowing” during film growth, which would cause higher void concentrations in the film . Areas at the center

of the wafer, to the contrary, would be impinged upon by much slower atoms, leading to less shadowing. As a result, thicker films would exhibit more densification upon annealing, which would appear as fringe bending in reflectometry heatmaps.

To conclude, optical reflectometry data proved to be a reliable supplement to optical microscopy. While the exact topography of damage in films was less apparent through reflectometry than microscopy, the existence of damage and its general nature was discernable. Optical reflectometry conclusively demonstrated that color changes in nondamaged films on 18F73 corresponds to a decrease in optical thickness, and not an increase like in 18PLD1. This finding more or less rules out silicate formation on sample 18F73.

Analysis of CHESS Diffraction Data

Synchrotron diffraction data was collected only for sample 18F73. As previously discussed, the anneal stripes on 18PLD1 were expected to have high amounts of silicon contamination, which may have presented as anomalous peaks in diffraction data. 18F114 and 18F118 did not possess well-characterized heating profiles due to the Ti sticking layer, so data concerning them could not easily be understood. Moreover, it is possible that the Ti sticking layer would introduce additional weak peaks to the data, making analysis more difficult.

Figure 3.13 represents a raw dataset outputted from the synchrotron diffraction experiment from the center of an anneal stripe. This figure is characteristic for the category of anneals above 780 ℃ and shorter than 1.5 ms. As can be seen, maximum intensity in the data takes the form of concentric arc. These arcs correspond to cones which satisfy Bragg's Law emanating from the substrate. An immediate finding from this data was that the film was polycrystalline and untextured. A single crystal film would present as a series of distinct diffraction spots, as opposed to continuous arcs.

Moreover, a textured film would not have continuous intensity across arcs, instead having areas of higher and lower intensity. Moreover, the lack of discernable spots evident in the arcs suggest that the crystals in this sample are of roughly the same size, with few significant outliers. The large rectangle in the center of the figure is caused by a dead zone in the detector, and does not indicate texturing in the film.

Figure 3.14 represents raw data captured from the center of a stripe that is characteristic of anneals with a peak temperature over 780 ℃ and a dwell longer than 1.5 ms. This

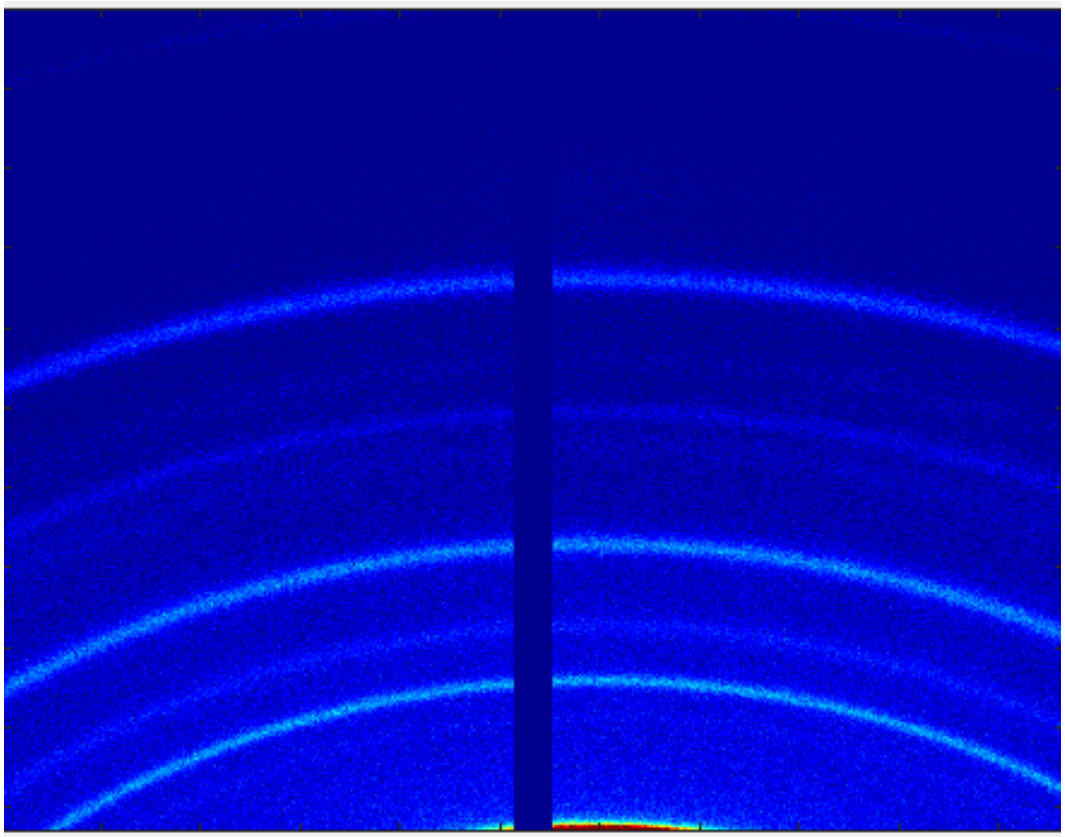

Figure 3.13: Raw XRD data captured from the center of a 300 μs 1200 °C anneal stripe.

data also suggests an untextured, polycrystalline film. However, a significant different is the appearance of the rings. Significant nonuniformity in intensity is notable across arcs. As the areas of heightened intensity appear irregular in shape and do not seem to

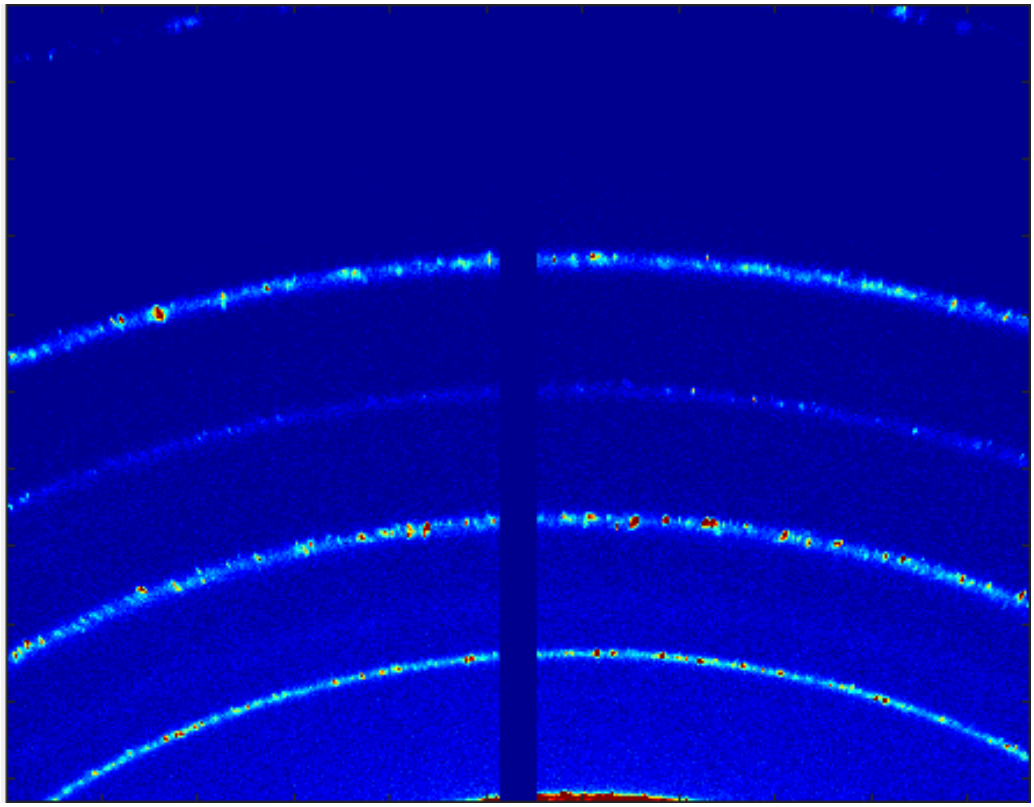

Figure 3.14: Raw XRD data captured from the center of a 2500 μs 1200 °C anneal stripe.

follow any pattern in location, they are not attributable to texturing in the film. A more likely explanation is that the areas of heightened intensity correspond to individual large crystal grains. Some areas of heightened intensity persist across three successive scan points, suggesting that grains at least 5 μm in diameter are present in these samples. However, the presence of a continuous diffraction ring underlying these more intense spots indicate that there also exists a large amount of small grained crystals in the film. The evidence on grain size from the raw diffraction data is consistent with the previous conclusions on the influence of dwell time on film structure. When dwells are long enough to allow areas of molten $BaTiO_3$ are able to coalesce, solidification fronts can form and allow large grains to form. Processes like competitive grain growth result in wide distributions of grain sizes in these anneal stripes, as confirmed by the raw

diffraction data. However, when dwells are to short for coalescence to occur, grains do not grow significantly and adopt a more uniform size distribution.

For more detailed analysis of the crystal structure of the anneal stripes, it was necessary to further process the raw diffraction data. To do this, an open source program known as pyFAI was employed to azimuthally integrate the data. This process essentially integrated the data about concentric rings to correlate intensity and diffraction angle. In this form, the diffraction arches appeared as distinct peaks about a specific angle. Figure 3.15 presents an example of this data transformation. Intensity will be presented as a function of q-vector length (q-length) in this study. Since diffraction angle is dependent on x-ray wavelength, commonly reported diffraction angles for materials are typically given for Cu-Kα radiation of 1.54 Å. However, since this study uses 1.0972 Å radiation, a conversion would be necessary to relate the obtained diffraction values to literature. As defined in Equation 3.1, q-length is only dependent on the d-spacing of atomic planes. Therefore, q-length can serve as a sort of common language for diffraction patterns of different wavelengths. Equation 3.2 provides the relationship between q-length and diffraction angle θ for a given x-ray wavelength λ.

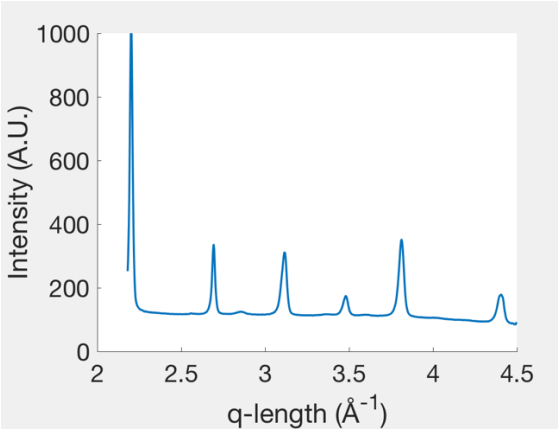

Figure 3.15: Azimuthally integrated diffraction data corresponding to the center of a 1200 °C 2500 μs anneal stripe.

$$Equation\ 3.1: q = \frac{2\pi}{d}$$

$$Equation\ 3.2: q = \frac{4\pi}{\lambda}\sin(\theta)$$

After integration, the data was background subtracted using a novel background subtraction technique developed by the Gomes Research Group at Cornell University. Additionally, the data was scrubbed of anomalously intense signals known as "zingers" and was normalized to a portion of the data noted to be free of peaks. As the total number of detected x-rays varied from integration point to integration, normalization was necessary to compare diffraction datasets. Peak-free areas were ideal for this purpose since their intensity is not affected by the laser anneal. Finally, the integration of the data was corrected for planarity issues using a Zr calibration wafer. More specific information regarding the planarity issue and its correction can be found in the Appendix. Figure 3.16 demonstrates a the final form of the data following all post processing.

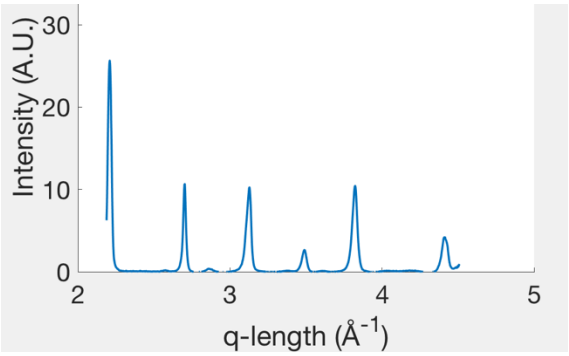

Figure 3.16: Azimuthally integrated and post-processed diffraction data for the center of a 1200 °C 2500 μs anneal stripe.

Manual inspection of all data suggests that all diffraction peaks correspond to either p-BTO or h-BTO structures. Further refinement of the data proved difficult. As demonstrated in Figure 3.17, all p-BTO peaks are in close proximity to an h-BTO peaks. Various mechanisms such as strain can cause peaks to shift off their literature suggested values, so classifying these "ambiguous" peaks as belonging to h-BTO or p-BTO was not possible. However, Figure 3.16 also demonstrates that h-BTO produces certain peaks that are not in close proximity to any p-BTO peaks. The presence of these unambiguous h-BTO peaks can be taken as concrete evidence as the presence of h-BTO in the area from which a diffraction dataset was taken. However, due to the issue of

discerning ambiguous peaks, the relative amount of p-BTO and h-BTO was not able to be determined. The small area under unambiguous h-BTO peaks relative to the ambiguous peaks' area suggest that no samples produced any areas of pure h-BTO, but rather h-BTO was always in mixture with p-BTO. Additionally, since the amorphous signal was convoluted with background signals such as air scatter, the background subtraction routine removed the amorphous signal from the dataset. As a result, it was not possible to determine the absolute crystallinity of the samples

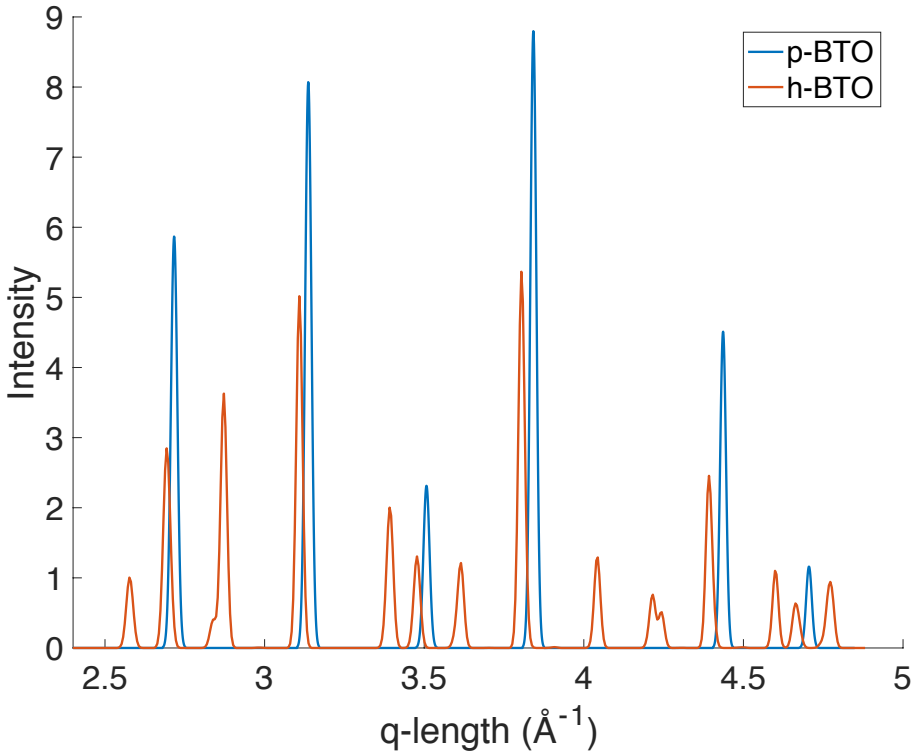

Figure 3.17: Diffraction peaks for powder p-BTO and h-BTO from literature.

Using the findings from manual inspection of the data, automated peak fitting was used as a means for phase identification. The process for the peak fitting consisted of first attempting to fit a gaussian in an area where p-BTO or h-BTO peaks would occur. If no good fit could be found in this area, the sample was presumed to be amorphous. Should

a peak be found, a second fit was performed on an area where an unambiguous hexagonal phase would occur. If this peak could be fit, the dataset was classified as having p-BTO and h-BTO. If no peak could be fit, the dataset was classified as containing p-BTO only. The results from this phase identification routine are presented in Figure 3.18. In this figure, the above described classification system was applied to a stripe as a whole. In other words, if h-BTO was detected anywhere on a stripe, the stripe was classified as containing h-BTO and p-BTO. As can be seen in the figure, the onset of crystallinity in the sample strongly corresponds to the damage threshold of 780 °C. This finding suggests that film damage was a necessary step in order to induce crystallization. An interpretation of this is that the substrate clamped the film, preventing the pre-crystallization volume expansion reported in literature. As a result, the film remained amorphous until damage occurred, at which point the film delaminated, became de-clamped, expanded and crystallized. It should also be noted that the peak locations for h-BTO differed from their literature locations. However, the literature locations for oxygen deficient h-BTO with the stoichiometry $BaTiO_{2.85}$ agree well with the experimental data. It is also possible that the shift of the h-BTO peaks is caused by tensile strain, and not off-stoichiometry.

Some crystallization is evident from the diffraction data on stripes that reflectance data suggest are undamaged, and vice versa. Although reflectance and diffraction data can be compared from the same stripe, the lateral line along which data was collected in each case is different. It is possible that damage did not occur on the tail ends of each stripe. If data was collected from the tail of a stripe in either the diffraction data or the reflectance data, the data could suggest crystallinity without damage or damage without crystallinity. Additionally, the film became completely detached from the substrate in many cases. It is possible that a piece of the film became dislodged from a damaged stripe and settled on an undamaged stripe. This could suggest damage or crystallinity in

an otherwise undamaged and amorphous stripe. Isolated cases notwithstanding, the data as a whole strongly supports a correlation between damage and crystallization.

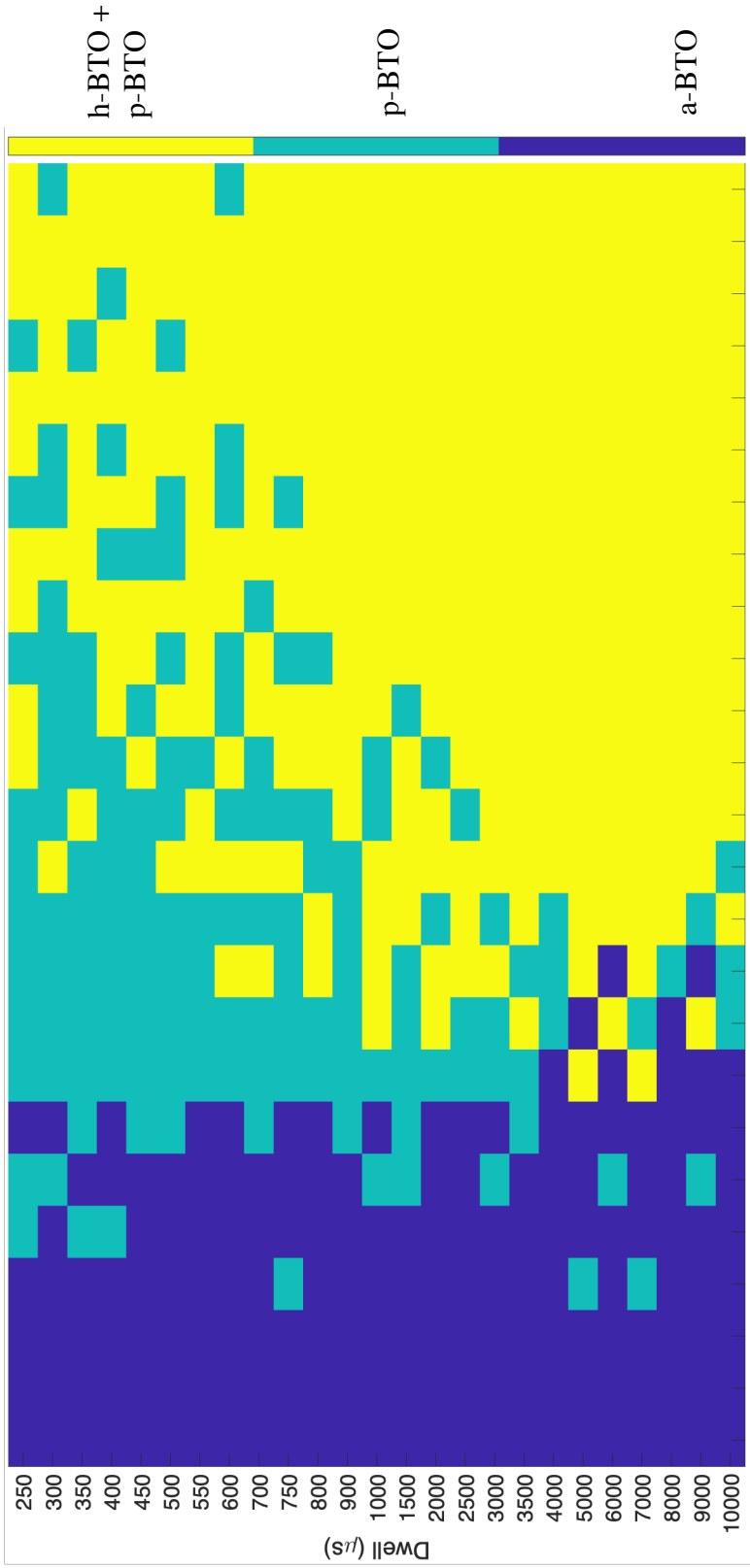

Figure 3.18: Phase mapping of sample 18F73 as a function of dwell and peak annealing temperature.

A behavior captured in the diffraction data, but not the reflectance data, is the onset of h-BTO in the film. As seen in Figure 3.18, film of short dwells just above the crystallization/damage temperature threshold are classified as pure p-BTO. This continuous area of pure p-BTO classification eventually breaks as longer dwells and higher peak temperatures are reached. Stripes containing some h-BTO are occasionally identified in this transition regime, but no firm onset threshold is evident. As a classification criterion for h-BTO involved the area under unambiguous peaks, it is likely that h-BTO is actually present in the transition regime, but the peaks were too weak to be identified. The more consistent h-BTO identification in the region containing long dwells and high temperatures indicates consistently stronger h-BTO peaks. In other words, the intensity of the h-BTO signal increases with time and temperature, suggesting h-BTO is favored in higher quantities under these conditions. Beyond phase identification, the diffraction data also shed light into the grain structure of the annealed films. Scherrer analysis was performed on each individual integration point on both unambiguous h-BTO peaks and ambiguous p-BTO or h-BTO peaks. Figure 3.19 provides a side by side comparison of the grain size evolution of these two peaks across a damaged, short dwell anneal stripe. As can be seen, the grain size decreases as distance from the center of the stripe increases. Although this stripe exhibited damage, and thus there exists limited knowledge of the exact temperature profile achieved in the film, the grain size roughly follows the ideal thermal profile. This result suggests that the deviation of the thermal profile in the film from the ideal is less than previously thought. Larger grain sizes are typically indicative of higher anneal temperatures. First and foremost, higher temperatures increase thermal diffusivity. This increase in diffusivity allows larger scale motion of atoms into nucleated crystals, resulting in larger grain sizes. Additionally, a higher temperature decreases the amount of undercooling in the material. This decrease lowers the driving force for crystal

nucleation and results in a lower overall numerical density of crystal nuclei. Transformation of the system into the crystal state is then concentrated into fewer nuclei, which achieve larger sizes than in a system with a high number of nuclei. Thus, the monotonic decrease in grain size as distance from the stripe center increases implies a monotonic decrease in peak temperature in the film as distance from the stripe center increases. This behavior is consistent for both peaks subjected to Scherrer analysis, suggesting no difference in the grain sizes that produced these peaks. However, the grain size from the ambiguous peak increases to a greater degree than the grain size from the unambiguous h-BTO peak. This finding suggests that the two peaks are not produced

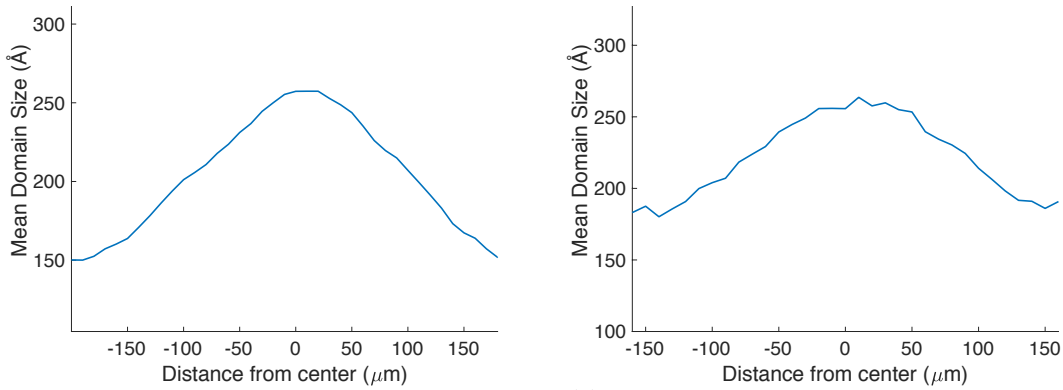

Figure 3.19: Calculated grain sizes across a 550 μs 1300 °C anneal stripe for an ambiguous peak (left) and unambiguous hexagonal peak (right).

from the same population of grains, indicating the presence of p-BTO. However, both p-BTO and h-BTO appear to increase in grain size with anneal temperature.

Interestingly, this grain size behavior does not occur at longer dwells. Figure 3.20 provides a similar comparison of calculated grain sizes for a damaged, long dwell stripe. Grain size seems to vary wildly, and follows no discernable trend across the stripe. Moreover, there is a lack of symmetry about the anneal center, clearly ruling out a dependence of grain size on the laser intensity profile. The grain size profile of the ambiguous peak also clearly diverges from the profile for the unambiguous h-BTO peak, which provides evidence that the analyzed peaks are not produced from the same

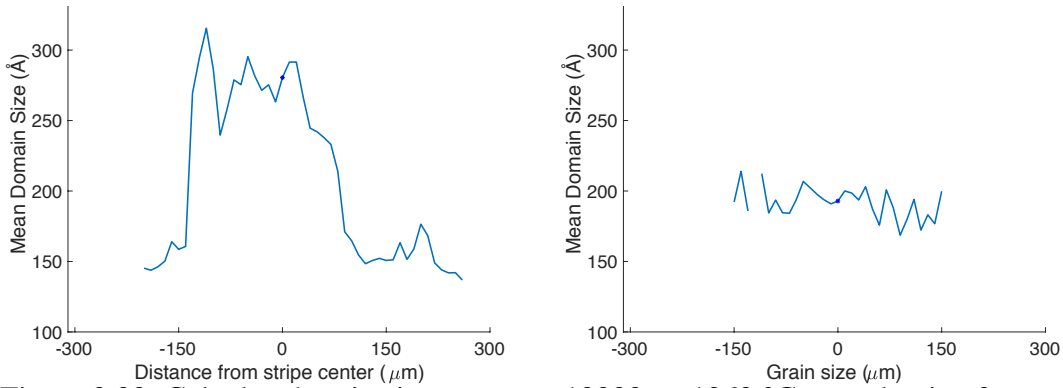

Figure 3.20: Calculated grain sizes across a 10000 μs 1260 °C anneal stripe for an ambiguous peak (left) and unambiguous hexagonal peak (right).

population of grains. This result suggests that the differences noted for damage in the reflectometry correspond to a difference in grain size.

The above finding suggests that the previously described damage mechanism may not be completely accurate. The close resemblance of the grain profile in shorter anneals to the ideal thermal profile could suggest that the films remained in thermal contact with the substrate throughout the anneal, and only became damaged after crystallization and grain growth occurred. Another explanation is that the films reached the ideal thermal profile and then delaminated, with crystallization and grain growth occurring before the delaminated film was significantly heated by the laser. If either of these explanations hold true, the films annealed with shorter dwells would not have achieved melt as previously thought. However, more data would need to be collected in order to confirm which explanation is correct.

Since the p-BTO grain sizes seem to vary between 15 and 30 nm in diameter, literature suggests that these are a mixture of tetragonal, cubic and orthorhombic crystals [5] [24] [25]. Literature also suggests that these nanograins of $BaTiO_3$ would have inferior dielectric properties when compared to bulk p-BTO, since low dielectric grain boundaries would act as dielectric "dead layers." However, these films would have

superior dielectric stability across a temperature ranges, as dielectric anomalies associated with rapid phase transitions would not occur.

Another interesting finding the diffraction data is the occurrence of "mobile peaks" on anneal stripes of high temperatures and short dwells. This phenomenon is best demonstrated through heatmaps similar to those used for reflectometry. Figure 3.21 provides a heatmap for a nominal stripe that does not exhibit mobile peaks. The vertical

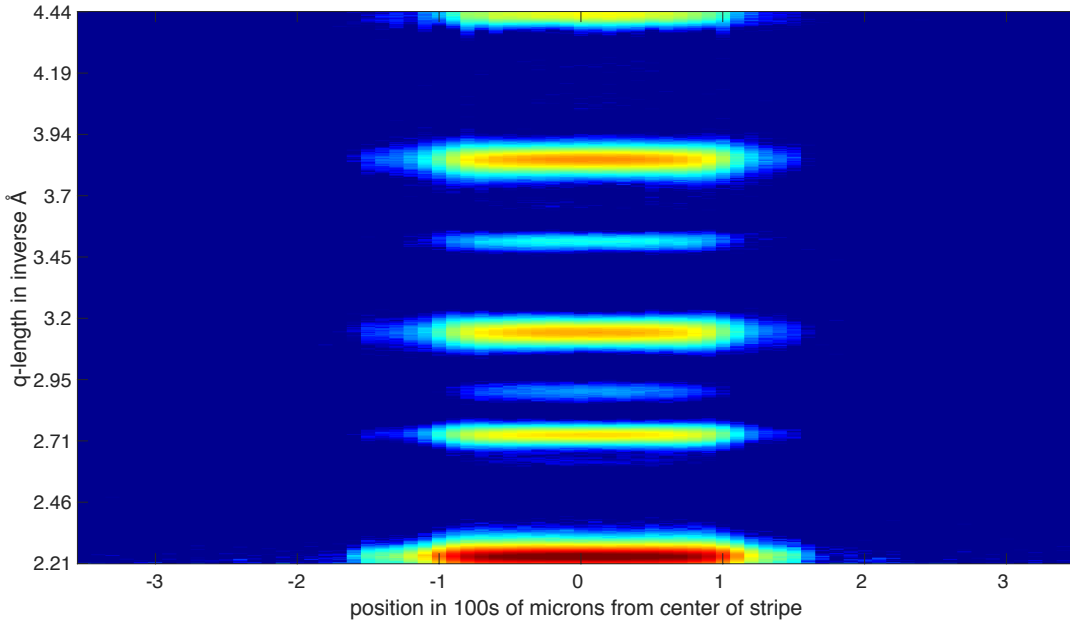

Figure 3.21: Diffraction heatmap for a 600 μs 1110 °C anneal stripe.

axis corresponds to q-length, and the horizontal axis corresponds to physical position on an anneal stripe. As can be seen, diffraction peaks present as continuous, straight bands across the width of the anneal region. Intensity of the bands tends to increase towards the stripe center, indicating increased crystallinity. This is behavior represents the appearance of a single crystal structure with consistent lattice spacings across an anneal. Figure 3.22 provides an example of a heatmap displaying mobile peaks. As can be seen, several of the bands bend upward in q-space towards the center of the anneal stripe, signifying a decrease in lattice spacing with temperature. These peaks also increase in intensity towards the center of the anneal, suggesting an increase in

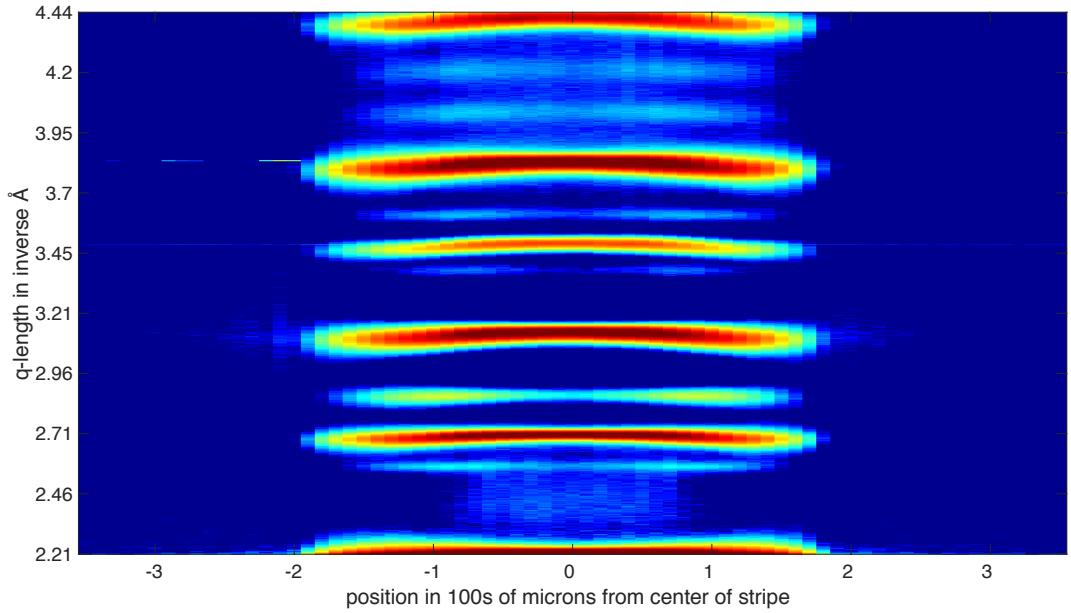

Figure 3.22: Diffraction heatmap for a 400 μs 1290 °C anneal.

crystallinity. However, bands that do not exhibit bending all decrease in intensity towards the center of the anneal. This behavior suggests that the atomic planes producing these reflections decrease in quantity towards the center of the stripe. Figure 3.23 provides a waterfall plot of several individual diffraction spectra from a stripe exhibiting mobile peaks. Additionally, spectra for oxygen deficient h-BTO and p-BTO from literature are provided for context. Oxygen deficient h-BTO has larger d-spacings than stoichiometric h-BTO, and the particular stoichiometry plotted shared the closest resemblance to the data at the onset of peak motion [10]. As can be seen, as distance to the center of the stripe decreases, the ambiguous peaks shift from h-BTO positions towards p-BTO positions. While this occurs, the unambiguous h-BTO peak remains stationary in q-space, but diminishes in intensity. Simply explaining this result as a higher percentage of p-BTO relative to h-BTO with increased anneal temperature is not entirely consistent. Since the literature location for p-BTO and h-BTO are far enough

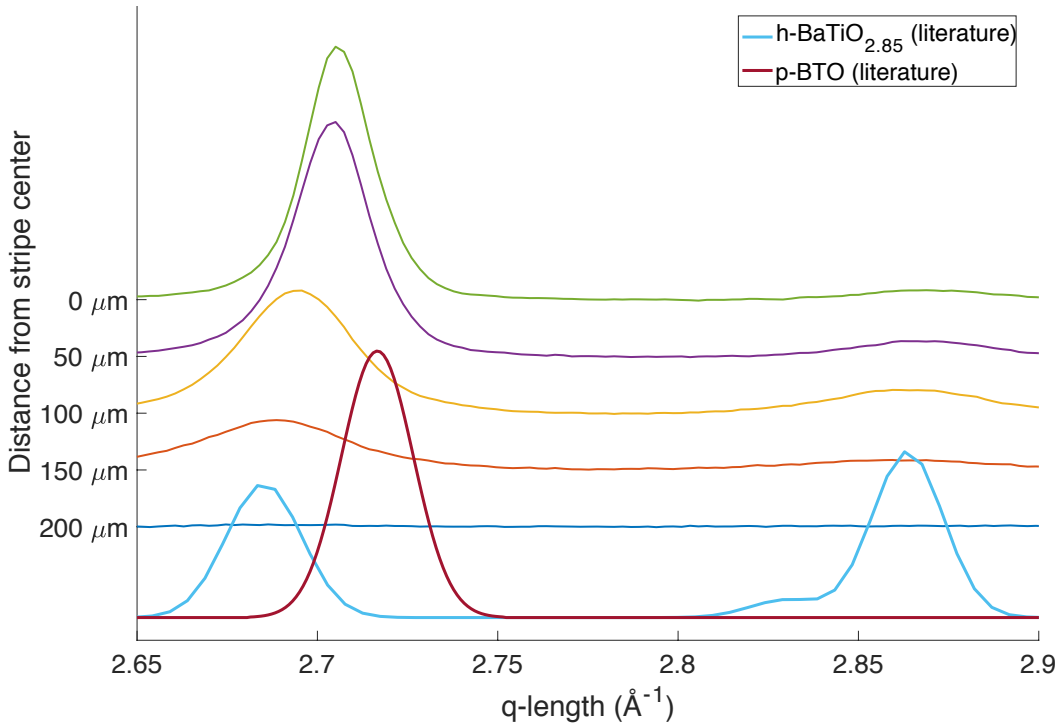

Figure 3.23 Waterfall plot of diffraction spectra from a 400 µs 1290 °C anneal with literature spectra for h-$BaTiO_{2.85}$ and p-$BaTiO_3$ included.

apart, one would expect coexistence of these two phases to present as a bimodal nature or shouldering in the ambiguous peak. However, visual inspection and automated curve fitting both fail to identify these characteristics in the ambiguous peaks.

Putting all things aside except for peak intensity, heatmaps containing mobile peaks provide firm evidence of decreasing h-BTO content as distance to the stripe center decreases. However, the lack of shouldering or bimodality in the ambiguous peak does not appear consistent with the presence of two phases of material. The apparent contradiction suggested here can be explained through a compressive straining of the p-BTO phase to adopt the lattice spacings of the h-BTO phase. If the p-BTO phase maintains its symmetry through this strain, no additional reflections would present. However, for example, the <200> reflection in the p-BTO phase would share location in q-space with the h-BTO <420>. As the h-BTO content decreases, the p-BTO grains become less strained and adopt a lattice spacing closer to the equilibrium value. This

explanation does not explain why the h-BTO lattice would not also strain to come closer to the p-BTO spacing. However, no other explanation is consistent with the collected data.

To conclude, synchrotron diffraction on 18F73 revealed that the damage identified through optical characterization shared a strong correlation with the onset of crystallization. Crystallization was observed to result in the formation of the h-BTO and p-BTO polymorph only. It was not possible to discern what phases of the p-BTO polymorph occurred due to the similarity in diffraction patterns for all p-BTO phases. As the collected diffraction data was fully consistent with h-BTO and p-BTO patterns, the presence of novel phases suggested by computational materials science was ruled out. Grain structure analysis suggests that films annealed under shorter dwells nominally follow the ideal temperature profile, and may not have melted. Additionally, the small size of the grains of p-BTO produced suggest the p-BTO crystals are of a distorted cubic structure that has orthorhombic symmetry. Some anneals at higher temperatures and shorter dwells presented diffraction data that show “mobile peaks.” This behavior can be explained by a transformation of h-BTO to p-BTO at higher temperatures along with a complex strain reaction in p-BTO grains in the presence of h-BTO.

Analysis of Atomic Force Microscopy

Micrographs of sample 18F73 produced via atomic force microscopy revealed interesting characteristics for undamaged stripes. Undamaged stripes had similar roughness values to unannealed films, so these films are continuous, smooth and suitable for microdevice fabrication. An interesting feature noted in these films is demonstrated in Figure 3.24, which is a topography image near the center of an undamaged stripe.. Thin lines, approximately 0.5 μm in width, hundreds of μm in length and 6 nm in height were observable on many undamaged stripes. These lines

exist roughly in the same direction as the annealing laser path, but were observed to diverge from parallel by as much as 15°. Since these lines were raised above the film surface, they are not explainable by cracking in the film. Moreover, the small vertical dimension of these lines are not consistent with contaminants. These lines are best explained as isolated regions of film buckling due to compressive stress. However, more atomic force microscopy on undamaged stripes should be performed in order to better understand these lines. A primary drawback of atomic force microscopy is the limited scan area size of 90 µm by 90 µm. Positioning the AFM over a new area required withdrawing the AFM tip and manually repositioning the sample. Additionally, there currently exists no reliable method to determine absolute position on a stripe. As such, measurements are only able to be classified as on a stripe, on a stripe edge or off a stripe. Because of this, precisely determining the location and orientation of lines was not possible.

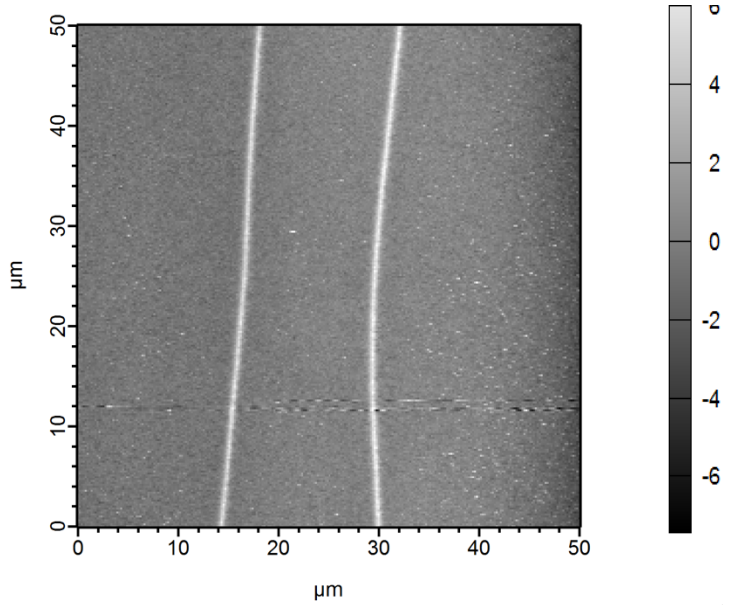

Figure 3.24: Atomic force microscopy height plot on a 500 μs 690 °C anneal stripe. The direction of the laser was from bottom to top.

CHAPTER 4: CONCLUSIONS AND DISCUSSION OF FUTURE WORK

Conclusions

This study explored the effects of millisecond scale laser spike anneals on $BaTiO_3$ thin films. In this study, $BaTiO_3$ thin films were grown on 0.01-0.02 Ω-cm p-type Si wafers via PLD and sputtering. Peak temperatures achieved in the substrates during individual anneals varied from 600-1400 °C, and anneal dwell times ranged from 250-10000 μs. Optical microscopy of films annealed on wafers without native oxide layers revealed significant reaction between the $BaTiO_3$ and the Si substrate, resulting in a transparent silicate layer. Optical microscopy on samples with native oxide layers revealed extensive film damage occurring above 780 °C, likely due to compressive film delamination. Profilometry of the films revealed significant roughening and delamination in the damage regions. Optical reflectometry revealed that undamaged films near the periphery of the wafer decreased in optical thickness during the anneal. Undamaged films near the center of the wafer did not demonstrate the same behavior.

Synchrotron x-ray diffraction demonstrated that the film crystalized at roughly the same temperature as the film damage onset. Film crystallization resulted in the appearance of both the hexagonal and perovskite polymorphs, although the perovskite polymorph appeared in greater purity at low temperatures and short dwells. Scherrer analysis of the diffraction data suggests that films of anneals shorter than 1 ms produced grains from 15-30 nm in diameter, with the smaller grains occurring at the periphery of laser anneal stripes and the larger grains occurring at the center of anneals. Longer dwells did not produce grains that followed a discernable trend. Diffraction analysis also demonstrated a possible relationship between perovskite phase lattice parameters and the quantity of hexagonal phase present in mixed phase regions.

Atomic force microscopy demonstrated that undamaged films did not display significant roughening. Although undamaged, films below 780 °C had several raised

ridges running along the laser anneal direction. The exact origin of these ridges in unknown, but they are speculated to be areas of film buckling due to compressive stress.

Future Work

As damaged films likely deviate from the expected temperature profile, the data in this study is not sufficient to propose a firm dwell-temperature phase map. Moreover, the rough nature of the damaged films makes electronic characterization impossible. Since damage occurred simultaneously with crystallization, the study of the electronic properties of crystallized $BaTiO_3$ is not possible with the current study. To remedy this, several changes to the experimental setup may be warranted. Firstly, a substrate that has a higher thermal expansion coefficient would decrease the stress that arises during the annealing procedure. Secondly, the films should be deposited at elevated temperatures in the future. Ideally, this temperature would be as high as possible without growing crystalline films. Combining these two methods would be ideal, as tensile stress in the film would be maximized. With this method, the film could be annealed to its deposition temperature before additional compressive stresses develop. After this point is reached, a high thermal expansion substrate would minimize the rate at which compressive stresses accumulate with temperature.

Another avenue to continue this experiment would be to study the undamaged, amorphous films. As evidenced by the compressive failures in crystalline films, the amorphous films in this study appear to undergo extreme expansion before nucleation. It has been reported when amorphous $BaTiO_3$ thin films are annealed to this expansion temperature under a strain gradient, the films develop macroscopic polarization without developing crystalline ordering. These films have been demonstrated to possess piezo-, pyro- and ferro-electric qualities up to the crystallization temperature of the film. These amorphous films may prove to be invaluable materials in applications such as FeRAM and temperature sensors. The high temperature stability of these polar amorphous

materials makes them particularly suited for high temperature applications. In previous studies, this strain gradient was generated by passing a passing point heat source across the film at the rate of a few mm/hr. The laser spike anneal thermal profile yields a much higher temperature and strain gradient. By adjusting the optics used in the laser spike anneal set up, the thermal gradient could be increased or decreased. Moreover, the laser spike anneal setup also allows for the exploration of the previously unstudied temporal dimension of this phenomenon. Future experiments on undamaged stripes should include piezoforce microscopy and pyroelectric effect measurements to quantify properties such as piezoelectric coefficient, switching voltage and pyroelectric coefficient as a function of temperature profile and dwell time. Moreover, such a study need not be limited to $BaTiO_3$. Other materials such as $SrTiO_3$, $BaZrO_3$ and $BiBaTiO_x$ have been documented to display macroscopic polarization in their amorphous phases and should be considered for study [26][27].

APPENDIX

Correction of Planarity in Synchrotron Diffraction Data

Analysis of integrated diffraction data revealed that peaks would drift around q-space from stripe to stripe independent of peak temperature and dwell. This behavior was eventually tracked to be dependent on the position of the stripe on the wafer. However, the dependence was not radially symmetric about the center of the wafer. Therefore, this effect was not attributable to film thickness variation. A better explanation was that the wafer was not perfectly coplanar with the X-Y stage during data collection. Figure A.1 demonstrates the implications of this planarity issue for a hypothetical planar deviation about the x-axis. As can be seen from the figure, a planarity error shifts the impact point x-rays on the sample, changing the sample to detector distance. When integrating raw synchrotron data, a fixed x-ray impact position is assumed to calculate diffraction angle. This drift in x-ray impact points causes peaks to appear to drift in q-space. Such drifts make peak identification impossible from stripe to stripe.

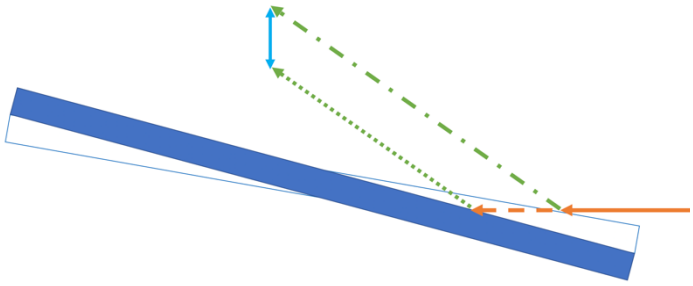

Figure A.1: Ideal experimental setup shows incoming x-rays in solid orange impacting the wafer outlined in blue and diffracting in dotted and dashed green. Actual experimental setup shows incoming x-rays in dashed orange impacting the solid blue wafer and diffracting in dotted green.

To correct this error, synchrotron data from a Zr metal film deposited on an Si wafer was collected. Synchrotron data was collected from this sample in a clock face pattern, as well as the wafer center. The integrated data showed the peaks drifting with position across the wafer, demonstrating the systematic origin of the drifting peaks. To remedy this, the elevation of each position on the wafer was calculated from the diffraction data.

Perfect planarity in this experiment would yield an elevation of zero for all locations. To calculate height at a position, an iterative approach was taken. By applying a transformation, given in Equation A.1, to the vector that relates intensity to q-length in the integrated data, the elevation of the sample at the data collection point was able to be artificially manipulated. In other words, one could introduce an artificial elevation in the data by changing the q-length vector. In this equation q_f represents a given q-length after transformation, q_i is the pretransformation q-length, λ is x-ray wavelength, d_{ideal} is the assumed sample to detector distance assumed in pyFAI, z is the artificial elevation imposed, and Θ_{stage} is the incident angle between the x-ray beam and the stage.

$$q_f(z) = \frac{\tan\left(2 * sin^{-1}\left(\frac{q_i * \lambda}{4 * \pi}\right)\right) * d_{ideal}}{d_{ideal} + \frac{z}{\tan\left(\Theta_{stage}\right)}}$$

By comparing the route-mean-square (RMS) deviation between the experimental peak locations and the literature peak locations as a function z in the equation above, and elevation could be identified for each data collection point that minimized the error. Figure A.2 demonstrates a plot that shows the change of RMS deviation between experimental and literature peak positions as a function of imposed elevation. This procedure was performed at multiple points across the Zr wafer and a polynomial surface was fitted to the computed points. This fitted surface is plotted in Figure A.3. Residuals between the surface and the calculated points were within 10 microns, lending credibility to the elevation calculations. The experimental data for 18F73 was then modified to take into account the planarity calculated from the Zr wafer. For the stripe most affected by planarity, the x-ray beam would overshoot its impact position by about 1.5 mm. While this overshoot is not enough to move the beam onto a different stripe, it

does introduce the peak drift seen in the data. It should be noted that this correction may introduce another error into the experimental data. If the Zr sample used to produce the planarity equation was strained its d-spacings would differ from literature systematically. As a result, the experimental data will artificially mimic the strain found in the Zr sample. This makes quantitative strain analysis impossible for the data on 18F73. However, the absolute position of peaks will remain constant across anneal stripes for a wafer. This allows for confident peak fitting, and was essential to the data workup. In the future, it would be prudent to include gold pads in a clock face pattern on a wafer via photolithography. Gold is self-annealing at room temperatures, so the effects of strain on data would be limited. Moreover, the pads would allow the equation of plane for an actual wafer to be calculated. This would eliminate any error that stems from discrepancies between two wafers.

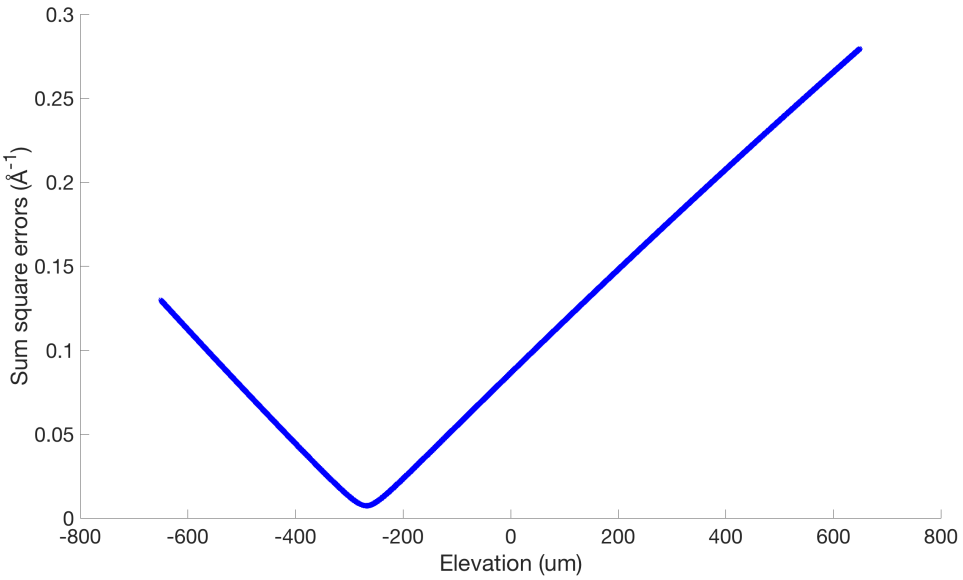

Figure A.2: Plot of sum square error between literature and experimental peak positions for metallic Zr as a function of sample elevation.

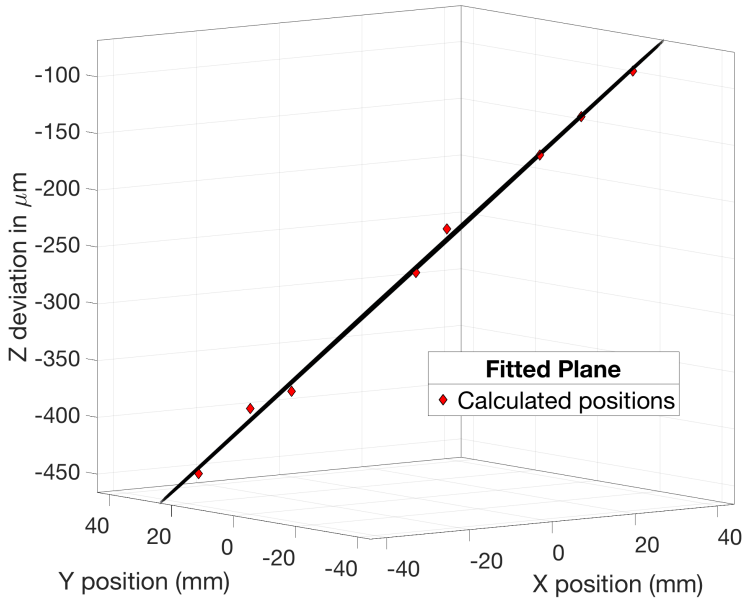

Figure A.3: Calculated elevations for the Zr sample overlaid with the plane fitted to these data.

References

[1] M. B. Smith *et al*., "Crystal Structure and the Paraelectric-to-Ferroelectric Phase Transition of Nanoscale BaTiO 3."

[2] G. H. Haertling, "Ferroelectric Ceramics: History and Technology."

[3] R. Pirc and R. Blinc, "Off-center Ti model of barium titanate."

[4] H. Ihrig, "The phase stability of BaTiO, as a function of doped 3d elements : an experimental study," 1978.

[5] M. H. Frey and D. A. Payne, "Grain-size effect on structure and phase transformations for barium titanate," 1996.

[6] S. Guillemet-Fritsch, Z. Valdez-Nava, C. Tenailleau, T. Lebey, B. Durand, and J.-Y. Chane-Ching, "Colossal Permittivity in Ultrafine Grain Size BaTiO3–x and Ba0.95La0.05TiO3–x Materials," *Adv. Mater.*, vol. 20, no. 3, pp. 551–555, Feb. 2008.

[7] R. Böttcher, E. Erdem, H. T. Langhammer, T. Müller, and H.-P. Abicht, "Incorporation of chromium into hexagonal barium titanate: an electron paramagnetic resonance study," *J. Phys. Condens. Matter*, vol. 17, pp. 2763–2774, 2005.

[8] R. Rajavaram, J. Park, and J. Lee, "Defect induced ferromagnetism in h-BaTiO3 synthesized from t-BaTiO3 by microwave heating," *J. Alloys Compd.*, vol. 712, pp. 627–632, Jul. 2017.

[9] A. Recnik and D. Kolar, "Exaggerated Growth of Hexagonal Barium Titanate under Reducing Sintering Conditions," *J. Am. Ceram. Soc.*, vol. 79, no. 4, pp. 1015–1018, Apr. 1996.

[10] D. C. Sinclair, J. M. S. Skakle, F. D. Morrison, R. I. Smithb, and T. P. Bealesc, "Structure and electrical properties of oxygen-deficient hexagonal BaTiO 3."

[11] I. Ebralidze, V. Lyahovitskaya, I. Zon, E. Wachtel, and I. Lubomirsky, "Anomalous pre-nucleation volume expansion of amorphous BaTiO3," *J. Mater. Chem.*, vol. 15, no. 39, p. 4258, Sep. 2005.

[12] J. Yu *et al*., "Giant Dielectric Constant of Hexagonal BaTiO 3 Crystal Grown by Containerless Processing."

[13] E. Wachtel and I. Lubomirsky, "Quasi-Amorphous Inorganic Thin Films: Non-Crystalline Polar Phases," *Adv. Mater.*, vol. 22, no. 23, pp. 2485–2493, Feb. 2010.

[14] P. Li, J. F. Mcdonald, and T.-M. Lu, "Densification induced dielectric properties change in amorphous BaTiO 3 thin films," *J. Appl. Phys.*, vol. 71, p. 5596, 1992.

[15] I. Ebralidze, V. Lyahovitskaya, I. Zon, E. Wachtel, and I. Lubomirsky, "Anomalous pre-nucleation volume expansion of amorphous BaTiO3," *J. Mater. Chem.*, vol. 15, no. 39, pp. 4258–4261, Oct. 2005.

[16] A. I. Frenkel, D. Ehre, V. Lyahovitskaya, L. Kanner, E. Wachtel, and I. Lubomirsky, "Origin of Polarity in Amorphous SrTiO 3," 2007.

[17] V. Lyahovitskaya, I. Zon, Y. Feldman, S. R. Cohen, A. K. Tagantsev, and I.

Lubomirsky, “Pyroelectricity in Highly Stressed Quasi-Amorphous Thin Films,” *Adv. Mater.*, vol. 15, no. 21, pp. 1826–1828, Nov. 2003.
[18] A. I. Frenkel, Y. Feldman, V. Lyahovitskaya, E. Wachtel, and I. Lubomirsky, “Microscopic origin of polarity in quasiamorphous BaTiO 3.”
[19] J. L. Wang *et al.*, “Ferroelectricity in a quasiamorphous ultrathin BaTiO 3 film,” *Phys. Rev. B*, vol. 84, p. 205426, 2011.
[20] G. Hautier, C. Fischer, V. Ehrlacher, A. Jain, and G. Ceder, “Data mined ionic substitutions for the discovery of new compounds,” *Inorg. Chem.*, vol. 50, no. 2, pp. 656–663, 2011.
[21] M. de Jong, W. Chen, H. Geerlings, M. Asta, and K. A. Persson, “A database to enable discovery and design of piezoelectric materials,” *Sci. Data*, vol. 2, p. 150053, 2015.
[22] Y. Nakata, “Pulsed-laser deposition of barium titanate films and plume dynamics,” *Appl. Surf. Sci.*, vol. 127–129, no. 1–2, pp. 650–654, 1998.
[23] W.-T. Liu, S. T. Lakshmikumar, D. B. Knorr, E. J. Rymaszewski, T.-M. Lu, and H. Bakhru, “Thermally stable amorphous Ba x Ti 2–x O y thin films,” *Appl. Phys. Lett*, vol. 66, p. 809, 1995.
[24] Y. Tan *et al.*, “Unfolding grain size effects in barium titanate ferroelectric ceramics,” *Sci. Rep.*, vol. 5, no. 1, p. 9953, Sep. 2015.
[25] Z. Zhao *et al.*, “Grain-size effects on the ferroelectric behavior of dense nanocrystalline BaTiO 3 ceramics.”
[26] D. Yu *et al.*, “Enhanced piezoelectricity in plastically deformed nearly amorphous Bi12-TiO20-BaTiO3 nanocomposites,” *Appl. Phys. Lett.*, vol. 109, no. 3, p. 032904, Jul. 2016.
[27] D. Ehre, V. Lyahovitskaya, A. Tagantsev, and I. Lubomirsky, “Amorphous Piezo- and Pyroelectric Phases of BaZrO3 and SrTiO3,” *Adv. Mater.*, vol. 19, no. 11, pp. 1515–1517, Jun. 2007.